The fundamental mechanisms of the Korotkoff sounds generation

Jérôme Baranger, Olivier Villemain, Guillaume Goudot, Alexandre Dizeux, Heiva Le Blay, Tristan Mirault, Emmanuel Messas, Mathieu Pernot, Mickael Tanter

▶ **To cite this version:**

Jérôme Baranger, Olivier Villemain, Guillaume Goudot, Alexandre Dizeux, Heiva Le Blay, et al.. The fundamental mechanisms of the Korotkoff sounds generation. Science Advances , 2023, 9 (40), pp.eadi4252. ⟨10.1126/sciadv.adi4252⟩. ⟨hal-04384466⟩

HAL Id: hal-04384466

https://hal.science/hal-04384466v1

Submitted on 10 Jan 2024

HAL is a multi-disciplinary open access archive for the deposit and dissemination of scientific research documents, whether they are published or not. The documents may come from teaching and research institutions in France or abroad, or from public or private research centers.

L'archive ouverte pluridisciplinaire **HAL**, est destinée au dépôt et à la diffusion de documents scientifiques de niveau recherche, publiés ou non, émanant des établissements d'enseignement et de recherche français ou étrangers, des laboratoires publics ou privés.

Distributed under a Creative Commons CC BY-NC 4.0 - Attribution - Non-commercial use - International License

APPLIED PHYSICS

The fundamental mechanisms of the Korotkoff sounds generation

Jerome Baranger[1]*, Olivier Villemain[1], Guillaume Goudot[1,2], Alexandre Dizeux[1], Heiva Le Blay[1], Tristan Mirault[2], Emmanuel Messas[2], Mathieu Pernot[1], Mickael Tanter[1]*

Copyright © 2023 The Authors, some rights reserved; exclusive licensee American Association for the Advancement of Science. No claim to original U.S. Government Works. Distributed under a Creative Commons Attribution NonCommercial License 4.0 (CC BY-NC).

Blood pressure measurement is the most widely performed clinical exam to predict mortality risk. The gold standard for its noninvasive assessment is the auscultatory method, which relies on listening to the so-called "Korotkoff sounds" in a stethoscope placed at the outlet of a pneumatic arm cuff. However, more than a century after their discovery, the origin of these sounds is still debated, which implies a number of clinical limitations. We imaged the Korotkoff sound generation in vivo at thousands of images per second using ultrafast ultrasound. We showed with both experience and theory that Korotkoff sounds are paradoxically not sound waves emerging from the brachial artery but rather shear vibrations conveyed in surrounding tissues by the nonlinear pulse wave propagation. When these shear vibrations reached the stethoscope, they were synchronous, correlated, and comparable in intensity with the Korotkoff sounds. Understanding this mechanism could ultimately improve blood pressure measurement and provide additional understanding of arterial mechanical properties.

INTRODUCTION

Blood pressure (BP) measurement is a medical act of prime importance in clinical practice. Among the pathologies whose diagnostics rely on accurate BP measurements, hypertension is one of the most prevalent in western countries, affecting up to one-third of adults (*1*), with a continuous relationship between BP and cardiovascular events (*2*). Incorrect diagnostics can lead to a higher risk of mortality due to overtreatment or lack of treatment (*3*, *4*). For this reason, regular BP measurement in the doctor's office is recommended whenever possible (*5*). Therefore, it is essential to develop noninvasive, robust, and widely available BP assessment methods (*6*). Nicolai S. Korotkoff brought one of the most substantial contributions in 1905 by discovering natural sounds from arteries that gave rise to the so-called auscultatory method. Briefly, it consists of wrapping a pneumatic cuff around the participant's arm. The cuff inflation above the systolic BP (SBP) occludes the brachial artery and hence stops the flow through the vessel. As the cuff is gradually deflated, blood flow is reestablished and accompanied by the so-called Korotkoff sounds (KSs), which can be heard with a stethoscope held over the brachial artery at the distal extremity of the cuff (*7*). SBP is measured when a first tapping sound is heard in the stethoscope (named KS phase 1), and diastolic BP (DBP) is reached when there is no sound anymore (KS phase V) (*7*). Despite the advent of automatic oscillometric devices (*8*) or Doppler techniques (*9*) not based on KSs, the auscultatory method remains the gold standard for noninvasive BP measurements (*10*–*12*). Therefore, the question of the origin of the KSs naturally arises.

Extensive studies have already proposed different theories for KSs origin. Among these, it was suggested that KSs are the result of a water hammer phenomenon in the brachial artery (*13*), a slight pressure dip shortly preceding the SBP upstroke (named the preanacrotic wave) (*14*–*16*), a collapse of cavitation bubbles in the arterial lumen (*17*), blood flow instability causing arterial wall fluttering (*18*) or "pistol shot" sounds (*19*), pulse wave distortion generating audible harmonics in arterial BP (*20*), and arterial wall vibrations modeled as dynamic instability (*21*, *22*) or observed by ultrasound (*23*–*25*). Despite the variety of potential mechanisms proposed by these studies, they all share a characteristic limitation in their methodology: They assessed the physical parameters (pressure, flow, and wall motion) at discrete locations along the artery. This limitation was mainly due to a constraint of most medical imaging systems, unable to track such transient phenomena in both space and time at thousands of frames per second.

Nevertheless, the reason for studying this phenomenon goes beyond simple scientific curiosity, as the auscultatory method has several shortcomings related to KSs themselves. In particular, DBP may be challenging to measure, as the KS is progressively muffled before silencing. Concerning SBP assessment, several limitations seem to exist in severely pathological cases, exposing to increased BP measurement variability (*26*). Uncovering the mechanism of KSs formation would provide a better understanding of their use in BP measurement.

Here, we managed to observe the entire section of the brachial artery affected by the arm cuff compression during KSs generation by leveraging the high spatiotemporal resolution of ultrafast ultrasound imaging (UUI). Unlike conventional devices using scanning focused beams of ultrasound, UUI systems use unfocused waves to reconstruct a wide field of view with very few transmits (*27*). The resulting frame rate can reach 10,000 images per second, to be compared with the typical 50 images per second of conventional methods. For this study, we designed a setup such that the brachial artery of healthy volunteers could be imaged along its longitudinal axis, under and outside the arm cuff, with a temporal resolution lower than 1 ms and sensitivity to motions as low as 3 μm. The measured physical parameters included arterial wall motion, tissue displacements, blood flow, and tissue stiffness. We compared them to

[1]Physics for Medicine Paris, Inserm, ESPCI PSL Paris, CNRS, Paris, France. [2]Université Paris Cité, Inserm UMR 970, PARCC, Vascular Medicine Department, Hôpital Européen Georges-Pompidou, Assistance Publique Hôpitaux de Paris, Paris, France. *Corresponding author. Email: baranger.jerome@gmail.com (J.B.); mickael.tanter@espci.fr (M.T.)

Downloaded from https://www.science.org on October 05, 2023

the KSs acquired simultaneously with an electronic stethoscope. These direct observations of artery and tissue displacements during the pulse wave propagation in the compressed artery in this spatiotemporal range provided an accurate physical and theoretical understanding of the KSs origin.

RESULTS

Tracking the arterial wall motion

We first investigated the role of arterial wall motion in the generation of KSs. Using a pressure cuff with a strap closure (*17*), we inserted a linear ultrasound transducer between the cuff straps to image the artery at three different locations and at different cuff pressure levels (Fig. 1A). At each transducer's location, UUI sequences were acquired. The sequences were triggered by the R wave of an electrocardiogram (ECG). Having this shared time origin made it possible to place side by side the acquisitions from different locations. This enabled to virtually reconstruct an ultrasound movie of the brachial artery over a 7.2-cm longitudinal segment, as if it had been acquired during a single cardiac cycle. From the same UUI dataset, both anatomic grayscale B-mode images and tissue Doppler axial velocities could be derived. Knowing the initial position of the arterial wall with B mode (Fig. 1B) and its dynamics with tissue Doppler, it was possible to follow the arterial walls along the cardiac cycle and to compare their motion with the stethoscope signal recorded at the distal cuff outlet.

Pulse wave and stethoscope signal

The results in Fig. 1 were acquired on a healthy 30-year-old male volunteer and at given cuff pressure P_{cuff} = 90 mmHg. Similar observations were made for all P_{cuff} values between SBP and DBP and are reported in fig. S1. This observation was characteristic, and similar results were found in all other healthy volunteers. The axial displacement and the velocity time courses of Fig. 1 (C and D) revealed the pulse wave propagation in the upper arterial wall following systolic heart contraction. For the rest of the article, all mentions to the arterial wall implicitly refer to the upper wall, the closest to the transducer surface. The pulse wave velocity (PWV) was derived from the delay between the different time courses and was of 1.2 m/s for this participant and cuff pressure.

The first notable result was the high wall velocity values (up to 26 mm/s in this example) as compared to a control situation without any external compression (~1 mm/s). We explain this by

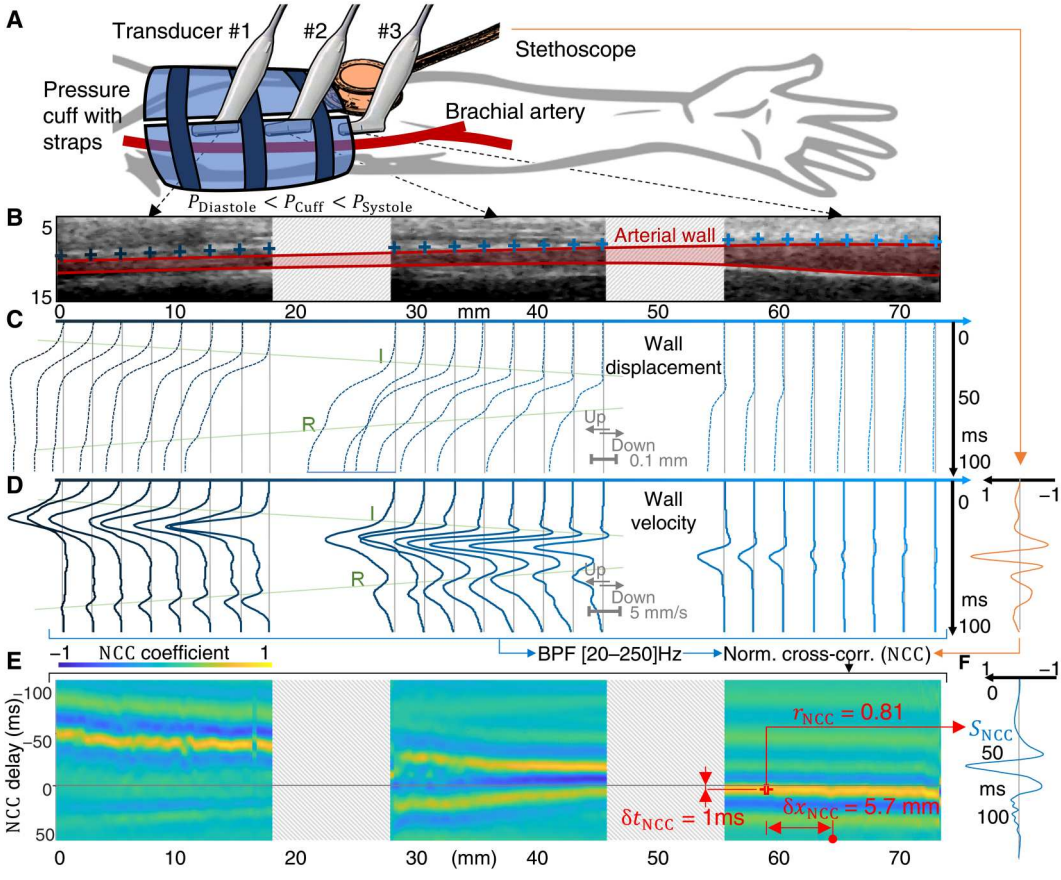

Fig. 1. Arterial wall velocity time course under the stethoscope is highly correlated to the KS. (**A**) Experimental setup. (**B**) B-mode images corresponding to the three transducers' positions, with dashed pads corresponding to the sections not imaged between each position. The brachial artery lumen is identified in red. The blue crosses identify 24 points in the upper wall. (**C**) Corresponding axial displacement and (**D**) axial velocity time courses. I, incident pulse wave; R, reflected wave. The KS from the stethoscope is plotted in orange. (**E**) NCC of the band-pass–filtered velocity time courses and the KS. r_{NCC} is the maximum of the NCC, corresponding to a distance δx_{NCC} to the center of the probe and to a signal delay of δt_{NCC}. The corresponding wall velocity time course S_{NCC} is reported in blue in (**F**).

Downloaded from https://www.science.org on October 05, 2023

considering the relationship between vessel compliance (defined as volume change with BP) and transmural pressure (defined as the difference between BP and cuff pressure). Without cuff compression, the BP radially stresses the arterial walls, but their constitutive collagen fibers are poorly stretchable in this tensile state and at physiologic BP ranges (*28*). This allows little volume change with pressure variation, in other words, low compliance and high stiffness [in the sense of functional stiffness as defined by Segers *et al.* (*28*)]. However, when the cuff pressure is in the range of SBP and DBP, it counterbalances the BP stress, bringing the artery to a less stiff and more deformable state. When the transmural pressure becomes negative (cuff pressure higher than SBP), the artery can even collapse. Therefore, around zero transmural pressure, the compliance of the artery strongly increases [see works by Drzewiecki *et al.* (*20*, *29*) for graphical illustrations], and the arterial stiffness strongly decreases, as will be shown here. Hence, in our experiment, when the pulse wave entered the artery segment compressed by the cuff, it reached a highly compliant artery and consequently generated strong displacements observed in Fig. 1C.

Second, the pulse wave appeared to be partially reflected at the distal cuff extremity [Fig. 1 (C and D), R line]. This phenomenon was also visible in movies S1 and S2 and was present as long as P_{cuff} was between SBP and DBP. The reflection occurred precisely where the artery transitioned from a state where it was under pressure from the cuff to its basal out-of-cuff state. In line with previous studies (*30*), we conjectured that the discontinuity of the artery stiffness and its diameter change at the extremity of the cuff induced this reflection.

Third, the evolution of the pulse wave time profile revealed a dispersive propagation. It was noticeable that the wavefront steepened as the distance to the proximal inlet of the cuff increased.

Last, the arterial wall velocity looked correlated and synchronous to the KS at the distal edge of the cuff, particularly right under the stethoscope. This was quantified using normalized cross-correlation (NCC) between the wall velocities' time courses and the KS. Signals were first band-pass–filtered in the low-frequency audible range where most KS energy lies (*31*). The maximum of the cross-correlation r_{NCC} was reached when comparing the KS and the arterial wall velocity at a longitudinal abscissa δx_{NCC}, defined as respect to the center of the ultrasound probe in its distal position (see Fig. 1A, position #3). This corresponded to the configuration where the probe was aligned with the stethoscope. The associated delay is denoted by δt_{NCC}, and the corresponding delayed wall velocity signal is denoted by S_{NCC} (Fig. 1, E and F). In the example shown in Fig. 1, δt_{NCC} = 1 ms and δx_{NCC} = 5.7 mm. This means that the wall velocity signal that was the most similar to the KS was almost synchronous with the KS and was located near the center of the transducer, that is to say, near the center of the stethoscope. The signal S_{NCC} reported in Fig. 1F was visually similar to the KS plotted in Fig. 1C, and the quantitative comparison gave a high correlation coefficient r_{NCC} = 0.81. While both wall velocities and displacements could be derived (Fig. 1, C and D), we focused on the wall velocity as the stethoscope sound is linked to the velocity of its diaphragm (*32*).

Correlation of wall velocity with KS

For the same participant, other S_{NCC} obtained with different values of P_{cuff} were compared to the KS recorded at these pressure levels (Fig. 2A). Qualitatively, the wall velocity was highly similar to the KS and displays the main features of the KS waveform. This trend was quantitatively confirmed by analyzing 23 KSs and corresponding UUI datasets acquired on $N = 6$ healthy volunteers at different pressure levels. The corresponding signals are displayed in fig. S2 and analyzed in table S1. On average, over the participant cohort, we respectively obtained the following values for the maximum of NCC, the location with respect to the center of the distal transducer, and the corresponding lag (± their SD): r_{NCC} = 0.87 ± 0.06, δx_{NCC} = −1.45 ± 5.88 mm, and δt_{NCC} = −1.49 ± 4.90 ms. The high r_{NCC} values suggested that KS and wall velocities had a comparable waveform. δx_{NCC} values near zero mean that the wall motion most similar to the KS was near the center of the stethoscope. Last, δt_{NCC} close to zero means that the wall motion corresponding to the KS was almost synchronous with it. From this quantitative analysis, we deduced that the KS has a strong spatial and temporal correlation with the arterial wall axial velocity under the stethoscope.

Wall velocity amplitude versus KS intensity

The previous NCC analysis helped us identify and locate the potential source of the KS. However, it did not reflect the relative intensity of KS and arterial wall velocities (Figs. 1, E and F, and 2A) due to the normalization of the signals. We wanted to answer the question of whether a loud KS corresponded to a high amplitude of arterial wall velocity (a faint KS and low wall velocity, respectively). To perform this comparison, we recorded several long audio tracks (60 s), each containing multiple KSs acquired at different cuff pressures, and compared them with the corresponding wall velocities acquired under the stethoscope (Fig. 2B). We estimated the signal intensities by extracting their root mean square (RMS) envelope (Fig. 2B) frequently used to measure audio power (*33*, *34*). By plotting the normalized KS envelope as a function of the normalized wall velocity envelope for each track, we quantitatively confirmed the linear relationship between wall motion intensity and audio power in the stethoscope (Fig. 2C and fig. S3 for individual track plots). The least-square fitting of Fig. 2C was $y = 0.921x + 0.045$ with r^2 = 0.88 (95% confidence interval: $y = 0.915x + 0.044$ and $y = 0.926x + 0.047$). In other words, the greater the arterial wall velocity, the louder the KS. Movie S3 (with audio) qualitatively shows this similarity between the KSs and the sounds derived from wall velocity.

Blood flow variation versus KS occurrence

As many past studies focused on the role of blood flow in KS generation, we proposed a simultaneous assessment of arterial wall velocity and blood flow in the segment located under the stethoscope. For a given participant and cuff pressure, tissue and blood signals were derived from the same UUI dataset (Fig. 2D). Doppler spectrogram reflecting blood flow was extracted from the vessel lumen (Fig. 2E), while the arterial wall motion right above that point was reported (Fig. 2F). Consistently with previous results, the KS signal was synchronous with the arterial wall motion. However, in this example, the blood flow only started to accelerate 38 ms after the onset of the sound. This substantial delay made any hypothesis linking KS and blood flow incompatible.

For some values of P_{cuff} lower than SBP, we observed that the artery was not fully collapsed under the cuff (see movie S1, 90 mmHg). Moreover, we did not detect any of the strong transient scattering event characteristics of cavitation bubbles imaged by ultrasound (*35*, *36*).

Downloaded from https://www.science.org on October 05, 2023

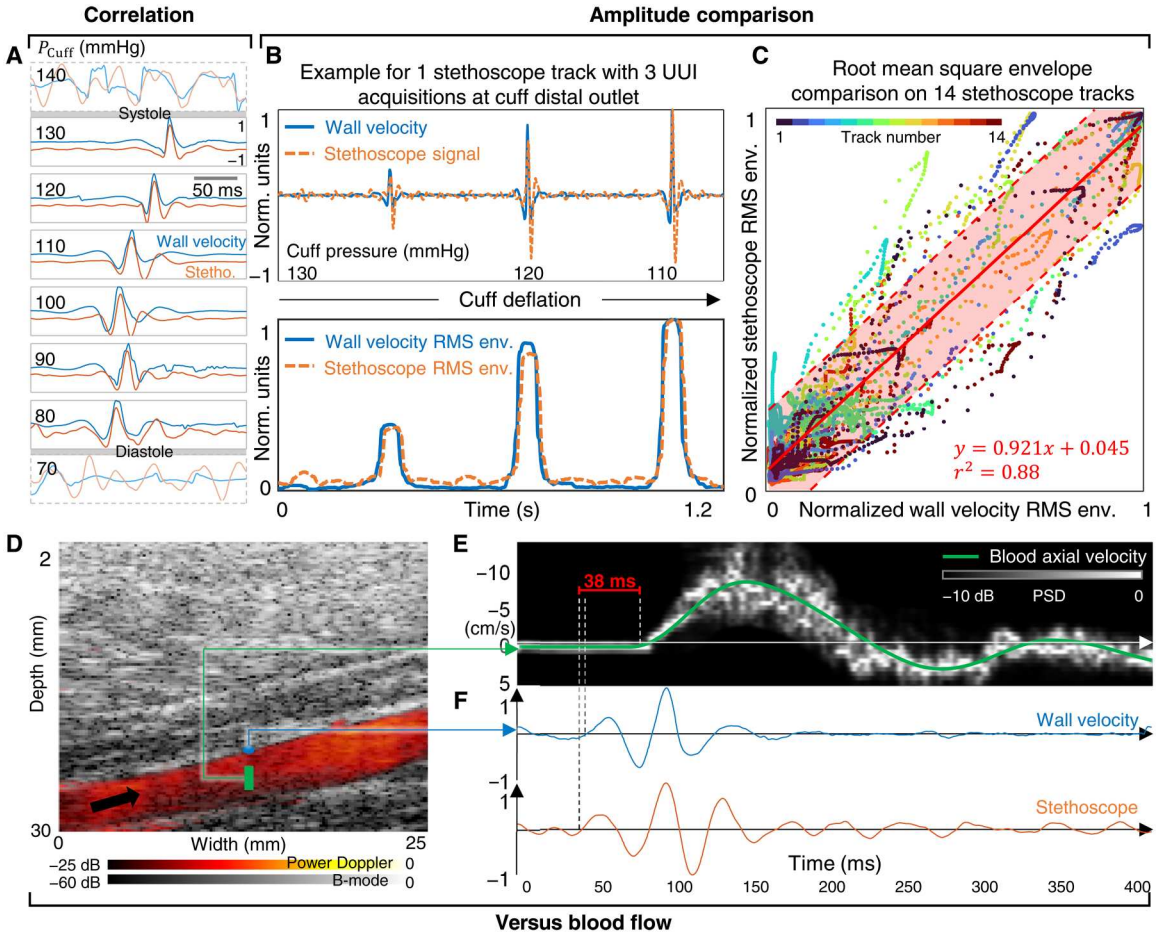

Fig. 2. Arterial wall velocity under the stethoscope is the source of KS. (**A**) KS at different pressure levels, compared to the associated wall velocity signal, slightly shifted upward for clarity. For cuff pressure above SBP (130 mmHg) or below DBP (80 mmHg), no KSs were heard by definition. (**B**) Time course (top) and RMS envelope (bottom) of a stethoscope track with three KSs, compared with the wall velocity under the stethoscope, during cuff deflation from 130 to 110 mmHg. (**C**) RMS envelope of stethoscope versus RMS envelope of wall velocity (14 stethoscope 60-s-long tracks, 40 KSs). Solid red line, fitted affine model; dashed red line, 95% confidence interval. (**D**) Power Doppler of the artery over tissue B mode. The cuff pressure was 80 mmHg near the DBP (70 mmHg for this participant). The blood flows along the black arrow. (**E**) Pulsed wave Doppler in the arterial lumen under the stethoscope and corresponding mean velocity. (**F**) Top: Wall velocity (in the audible range) acquired at the blue circle in (D). Bottom: KS recorded in the stethoscope.

Sound propagation or shear propagation?

Previous results demonstrated the link between the arterial wall velocity during the pulse wave propagation and the KS. The mechanism of the transmission of this wall vibration to the stethoscope had yet to be investigated. Intuitively, all past studies inferred that the source of the KS was located in the artery or in its walls and that a sound wave was radiating from that source to the nearby stethoscope. However, this mechanism is incompatible with our results. The NCC results of Fig. 1E showed that even for arterial segments located near the proximal edge of the cuff, the wall velocity signals exhibit high NCC values with the KS in the audible range, but these high NCC values were associated with high NCC temporal lags. For instance, the wall velocities at the abscissa 30 mm reached a maximum NCC coefficient of 0.78 for an NCC lag of −25 ms. In other words, the vibrations of the proximal segments of the artery under the cuff and the KS were similar but temporally distant by dozens of milliseconds. With the hypothesis of a sound wave between the KS source and the stethoscope and a typical speed of sound of 1540 m/s in human soft tissue (*37*), we should have heard the KS only 20 μs after the pulse wave had penetrated under the cuff. Thus, there was a discrepancy between this sound-wave hypothesis and our NCC analysis. We propose another mechanism compatible with the observed timings: radial shear motion radiated in tissues by the arterial pulse wave (Fig. 3A).

From Fig. 3 (C and E) and movies S1 and S2, we observed that the arterial wall motions were transmitted to the surrounding tissues [see movie S4 for a three-dimensional (3D) representation]. These radial tissue displacements propagated longitudinally. Therefore, they constituted shear displacements in tissues whose speed was driven by the PWV. This was confirmed by a shear-wave time-of-arrival map (Fig. 3C), with the probe in the middle of the cuff. The iso-delay lines were almost orthogonal to the artery axis, which means that for a given abscissa along the artery, the wall motions were transmitted to the tissue in the radial direction (Fig. 3E). We hypothesized that these radial shear vibrations were converted into compression when they reached the stethoscope

Downloaded from https://www.science.org on October 05, 2023

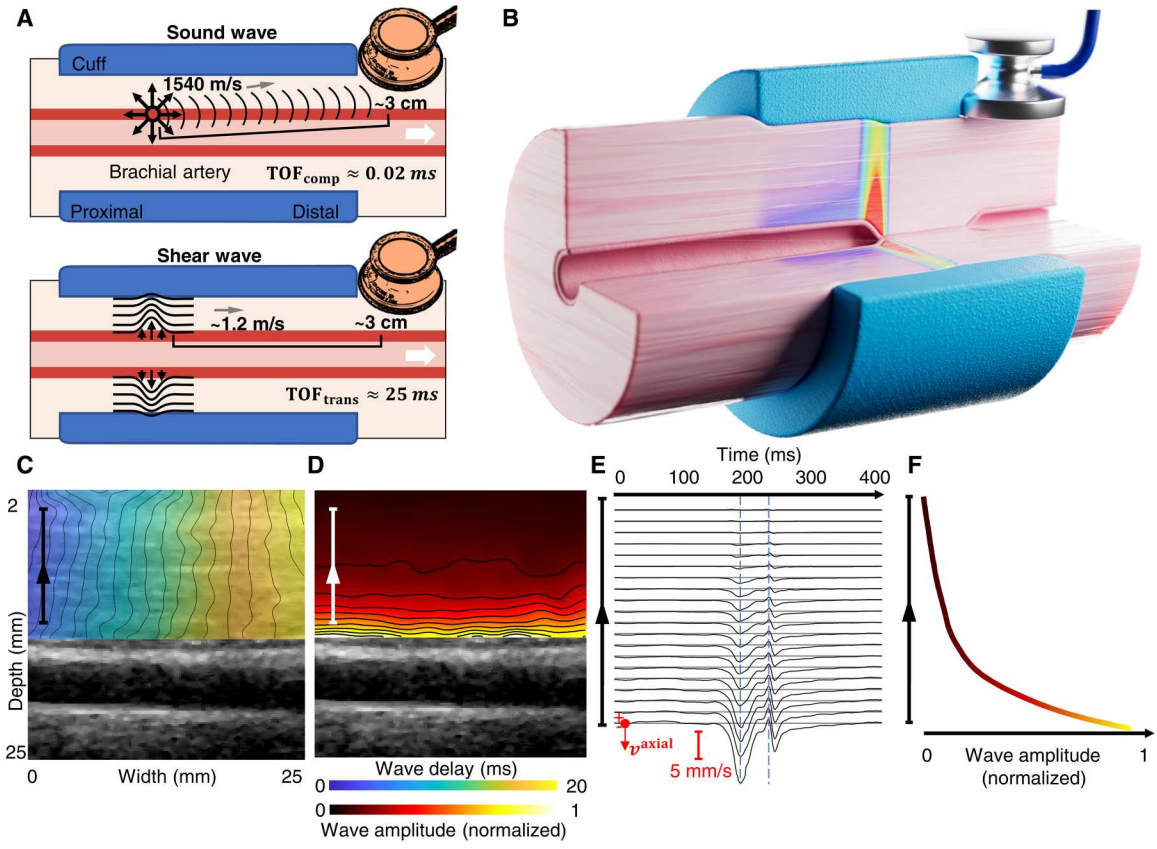

Fig. 3. The radial evanescent shear wave mechanism. (**A**) Time-of-flight (TOF) comparison under the hypotheses of a sound wave (top) and shear wave (bottom). (**B**) 3D representation of the pulse wave in the artery and of the radial evanescent shear wave in the tissues. (**C**) Time of arrival of the shear wave in the tissue, overlaid on the anatomical image. Zero delay is set as the bottom left corner of the map. Black isolines of delay are plotted every 1 ms. Transducer inside the cuff inflated at 100 mmHg, between SBD and DBP. (**D**) Map of the RMS wave amplitude, normalized by the maximum over the field of view. Black isolines of amplitude are plotted with a step of 0.1. (**E**) Axial velocity time courses of several tissue points, distributed along the segment drawn in (C) and (D). (**F**) Corresponding normalized RMS wave amplitude.

diaphragm, hence creating the KS. As the PWV was much slower than the speed of sound (range of meter per second versus kilometer per second, respectively), this mechanism explains the previously stated paradox: The wall velocity at abscissa 30 mm was highly similar to the KS waveform (i.e., high NCC values) but occurred 25 ms earlier than the KS. This 25-ms lag was precisely the time needed by the shear wave to propagate from the considered abscissa to the stethoscope, located approximately 30 mm farther in the longitudinal direction, with a PWV of 1.2 m/s (Fig. 3A). Note that our results did not rule out the possibility of mode conversion of the shear wave into a compression wave, but considering the relative intensity and timings of the KS and the pulse wave, we can say that if such mode conversion occurred, then it was not the source of the KS.

Evanescent radial shear displacements

To better understand the propagative properties of these shear displacements, we independently measured the stiffness of the muscle surrounding the artery using shear wave elastography (SWE) (*38*). With the same ultrafast ultrasound scanner, controlled shear waves were induced in the tissue by applying an acoustic radiation force. SWE consists of measuring the speed of these induced shear waves, denoted by c_{SWE}, and to convert them into Young's modulus, denoted by E. The values were collected for several cuff pressure levels for tissue regions located inside the cuff and distal to the cuff (see fig. S1). We observed that when the cuff pressure was above 80 mmHg, the stiffness of the compressed tissue increased above 110 kPa, corresponding to $c_{SWE} \approx 6$ m/s, whereas it was 50 kPa without compression ($c_{SWE} \approx 4$ m/s). Put differently, during an increase of cuff pressure, surrounding tissues stiffened, whereas the arterial wall softened (PWV from 5 m/s down to 1.5 m/s). The radial shear motion generated in the tissue by the pulse wave was therefore in a subsonic-like regime: Its speed was much slower than the speed of induced shear waves freely propagating in the same material and driven by the arterial pulse wave. Thus, this radial shear wave cannot be considered as a classical shear wave generated into tissue, but it corresponds to an evanescent wave with a radial exponential decay, jointly propagating with the pulse wave of the arterial wall (*39*). This radial exponential decay was confirmed in Fig. 3 (D and F). The evanescent nature also explains why the tissue and arterial wall motions were synchronous in the radial direction (Fig. 3, C and E).

Wall velocity frequency content

Now that we showed that KS originated from arterial wall velocity and was transmitted to the stethoscope through an evanescent radial shear wave mechanism, we investigated how the pulse wave

Downloaded from https://www.science.org on October 05, 2023

propagation under the cuff affected the sound characteristics. The space-resolved spectral analysis (Fig. 4A) confirmed the previously conjectured nonlinear propagation of the pulse wave. Its fundamental frequency progressively shifted from 20 Hz in the proximal region to 40 to 50 Hz at the distal outlet of the cuff, which corresponded to the typical center frequency of KSs (*31*). The good accordance between the wall velocity spectrum at cuff distal edge and the stethoscope signal spectrum led us to conclude that the frequency content of KSs was driven by the dispersive propagation of the pulse wave under the cuff. Although wall velocity signals in proximal regions already had audible components close to the KSs, only wall velocity signals in distal regions of the cuff exhibited the full spectrum of the KSs.

Nonlinear propagation of the pulse wave: Theory

We also see in Fig. 4 that the power spectral density (PSD) of the first harmonic increased with propagation distance (see for instance Fig. 4A, 90 mmHg). This translated the steepening of the wavefront that was previously observed in Fig. 1D. We can define a Mach number for the pulse wave as the ratio between the maximum wall velocity and the propagation speed of the pulse wave. Typically, wall velocities reached tens of centimeters per second within the pressurized cuff pressure to be compared to the basal situation without cuff (~1 mm/s). On the contrary, PWV was down to 1 m/s with cuff pressure and up to 5 m/s without cuff. This means that the Mach number typically increased from 10^{-3} without cuff to 10^{-1} with cuff. Consequently, with this 100-fold increase of the Mach number, high-order nonlinear effects become important and affect the pulse wave shape.

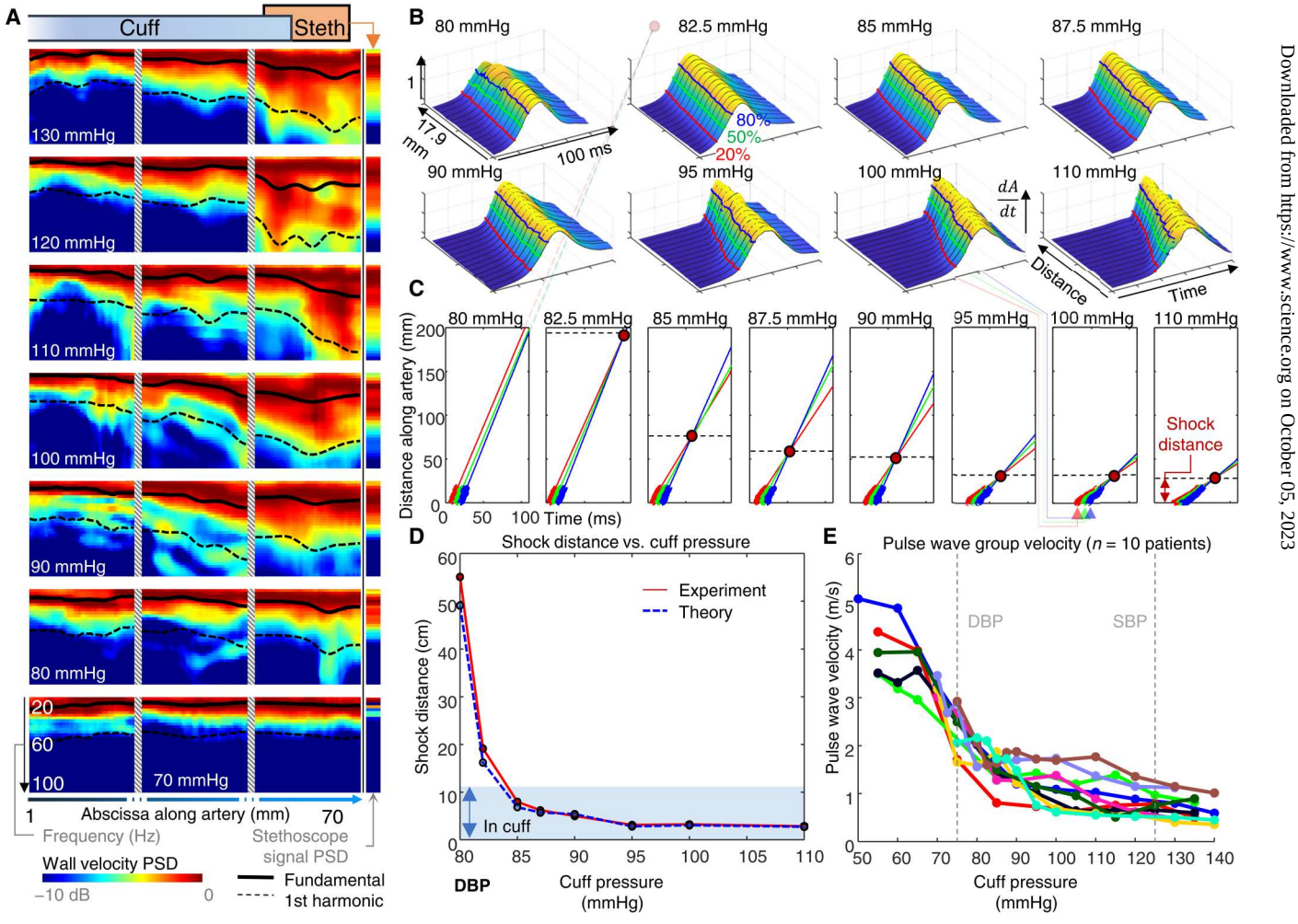

Fig. 4. Nonlinearity of pulse wave propagation versus cuff pressure. (**A**) Power spectral density (PSD) of the arterial wall velocity for each abscissa along the artery and for different cuff pressures, averaged over $N = 6$ participants. The dashed gray pads (not to scale) mark the nonimaged areas between each transducer positions. The corresponding stethoscope signal PSD is shown on the right side. (**B**) Relative variation of the arterial lumen area, as a function of time and abscissa along the artery, for a given participant at eight cuff pressure levels. Each surface was normalized by its maximum dA/dt value. Three characteristic curves at 20, 50, and 80% of the maximum are plotted in red, green, and blue, respectively. (**C**) Projection of the characteristic curves on the distance-time plane. Data points appear as thick dots in the range of 0 to 17.9 mm of the graph. Linear regressions are plotted in solid red, green, and blue. (**D**) Theoretical and experimental shock distances as a function of cuff pressure. (**E**) Ten pulse wave group velocity curves plotted for 10 participants, with averaged DBP and SBP values.

Downloaded from https://www.science.org on October 05, 2023

We derived the theory for this nonlinear propagation of the pulse wave in arteries located under the cuff (see Materials and Methods). For this, we used the linearized equations of axisymmetric flow in a flexible tube by considering small perturbations

$$\begin{aligned}\partial_t A + \partial_x Q &= 0\\ \partial_t Q &= -\frac{AK_p}{\rho}\frac{dP}{dA}\partial_x A\end{aligned} \tag{1}$$

where A is the tube area, P is the arterial pressure, ρ the blood density, and K_p is a constant proportional to the bending stiffness. The link $\frac{dP}{dA}$ between the arterial pressure P and area A is strongly depending from the nonlinear elastic properties of the arterial wall. By using the Laplace law, one can show that the transmural pressure p_{tm} is linked to the wall stress σ (force per unit area) and artery radius R as $p_{\mathrm{tm}} = \frac{\sigma h}{R}$, with h the wall thickness. We propose then to derive σ from the acoustoelasticity theory by expressing the stress field as a function of the Piola-Kirchhoff stress tensor and to develop the elastic energy density in the fourth-order approximation as first introduced by Landau and Lifshitz (*40*). We obtain the dependency of transmural pressure as a function of the area A

$$\begin{aligned}p_{\mathrm{tm}} = \mu\frac{h}{\pi {R_0}^3}(A-A_0) + \left(\frac{A_L}{4}-\frac{3D_L}{2}\right)\frac{h}{\pi^2 {R_0}^5}(A-A_0)^2\\ + \frac{D_L}{2}\frac{h}{\pi^3 {R_0}^7}(A-A_0)^3\end{aligned} \tag{2}$$

with μ and A_L being the expansion of Landau and Lifshitz theory and the coefficient D_L identified as the fourth-order elastic constant (*41*). The Landau coefficient A_L determines the nonlinear shear stress (or behavior), while D_L is required to describe nonlinear distortion of shear mechanical waves in finite amplitudes. A_0 and R_0 are the area and radius of the constrained artery in the absence of arterial pulse, respectively. By calculating dp_{tm}/dA, one obtains the nonlinear propagation equation for the arterial pulse wave under the cuff

$$\begin{aligned}&\partial^2_{tt}A\\ &-\partial_x\left\{\left[\mu\frac{h}{\rho R_0}+\left(\frac{A_L}{4}-\frac{3D_L}{2}\right)\frac{2h}{\rho\pi {R_0}^3}(A-A_0)+\frac{3D_L}{2}\frac{h}{\rho\pi^2 {R_0}^5}(A-A_0)^2\right]\partial_x A\right\}\\ &=0\end{aligned} \tag{3}$$

We introduce the speed for zero stress induced by the arterial pulse, ${c_0}^2 = \frac{\pi h\mu}{\rho R_0}$, where $\mu = \mu(P_{\mathrm{cuff}})$ should be considered as the shear modulus of the vessel under the static cuff constraint in the absence of arterial pulse. When neglecting nonlinearities, c_0 is given by a modified Moens-Korteweg equation

$$c_0 = \sqrt{\frac{Eh}{3\rho R_0}} \tag{4}$$

considering $E = 3\mu$ in soft solids and a thin-wall approximation. Note that c_0 depends on the static cuff pressure P_{cuff}. Increasing the cuff pressure progressively counteracts the diastolic arterial BP P_{diast}. It results in a very low transmural pressure corresponding to a softening of the artery segment under the cuff and a decrease of c_0. Equation 3 can be factorized into two counterpropagating terms and leads to the propagation equation toward the increasing x values

$$\begin{aligned}&\partial_t A\\ &-\left[c_0+\left(\frac{A_L}{4}-\frac{3D_L}{2}\right)\frac{c_0}{\mu\pi {R_0}^2}(A-A_0)+\frac{3D_L}{4}\frac{c_0}{\mu\pi^2 {R_0}^4}(A-A_0)^2\right]\partial_x A\\ &=0\end{aligned} \tag{5}$$

Equation 5 can be seen as a modified Burgers equation for the propagation of the pulse wave under the cuff. The propagation speed depends on the local radius and leads to a cumulative distortion of the pulse wave during the propagation under the cuff. By using the characteristics theory, we can derive the shock distance due to the nonlinear propagation of the arterial pulse

$$L_S^{\mathrm{theory}} = \lambda_{\mathrm{pw}}.\frac{\pi\mu(p_{\mathrm{cuff}}-p_{\mathrm{diast}})}{\left(\frac{A_L}{2}-3D_L\right)}.\frac{{R_d}^2}{R_{\max}^2-{R_d}^2} \tag{6}$$

where λ_{pw} is the wavelength of the pulse wave under the cuff, R_d is the minimal diastolic radius, and $R_{\max}$ is the maximal radius. We show that the shock distance L_S^{theory} directly depends on the ratio between the linear elastic coefficient in the absence of the arterial pulse and the nonlinear elastic parameters at maximal distortion during the pulse wave propagation under the cuff multiplied by the squared ratio between R_d and $R_{\max}$. When $\mu(P_{\mathrm{cuff}})$ becomes very low and nonlinear elastic properties are high, it results in a very short shock distance L_S^{theory} and the generation of harmonics in the radial shear wave (Fig. 4A). As the Landau coefficients A_L and D_L are unknown for arteries, we derived a typical value for linear/nonlinear elastic ratio of Eq. 6 by fitting the parameters of Eq. 2 to the experimental curve $p_{\mathrm{tm}} = f(A)$ of Drzewiecki *et al.* (*29*). Knowing the radius R_d and $R_{\max}$ at the different cuff pressures from our ultrasound data, we finally obtained L_S^{theory}.

Pulse wave shock distance

Qualitatively, we can see this shock as the moment where the "tail" of the pulse wave catches up with the "head." This phenomenon was visible in Fig. 4B for cuff pressure of 100 and 110 mmHg: After a few millimeters of propagation, the wavefront steepens and becomes almost vertical. The theory of characteristics states that this shock is reached when characteristic curves of equivelocity intersect. Three characteristics curve corresponding to equivelocities of 20, 50, and 80% of the maximum velocity were reported in Fig. 4B for several cuff pressure on a given participant. Figure 4C shows the projection of these curves on the distance-time plane, with a linear regression for each curve. These fitted lines intersected at a distance L_S^{exp} that was the experimental shock distance. Figure 4D compares L_S^{theory} and L_S^{exp} and shows a good agreement between theory and experiment. Another example with a second participant is provided in fig. S3.

Pulse wave group velocity

Essentially, this nonlinearity results in different phase velocities for the multiple frequency components of the pulse wave. This explains the spectral dispersion and distortion observed in Fig. 4A. From Eqs. 3 to 6, we can also see that the velocity at zero stress depends on the initial artery radius and, consequently, of the static cuff pressure. The consequence is that in addition to the dispersive

Downloaded from https://www.science.org on October 05, 2023

propagation that causes the spreading of the pulse wave, the velocity of the pulse wave envelope (namely, its group velocity) also decreases with cuff pressure. The group velocity of the pulse wave corresponds to what is commonly called the PWV. This theoretical decrease of PWV with cuff pressure was observed in previous studies (*21*, *25*) and confirmed with UUI (Fig. 4E). The PWV curve had a sharp transition around DBP (70 to 80 mmHg for our cohort, N = 10 healthy volunteers aged 24 to 32 years old) and reached a plateau around 1.1 m/s for a cuff pressure above DBP. PWV was still measurable for a cuff pressure slightly above SBP as partial opening of the artery was observed at the proximal part of the cuff (see also movie S2 for P = 140 mmHg).

DISCUSSION

From these results, we propose the following theory for the origin of the KSs: (i) By decreasing the transmural pressure and, therefore, the brachial artery stiffness, the pressure cuff slows down the pulse wave and amplifies the local arterial wall displacements. (ii) The resulting high velocity of the arterial wall compared to the propagation speed of the pulse wave results in a highly nonlinear propagation regime under the cuff transferring wave energy from very low, barely audible frequencies to a higher-frequency audible content. (iii) These nonlinear vibrations radiate into the surrounding tissues, where they form shear displacements with an amplitude exponentially decaying with the distance to the arterial wall. These tissue vibrations propagate jointly with the arterial pulse wave. (iv) When these shear tissue displacements reach the stethoscope (at the distal edge of the cuff), they are converted into compressional displacements within the stethoscope diaphragm and create the KS.

Beyond previous hypotheses

Our observations refute some of the previous hypotheses for KSs origins. In particular, our results seem incompatible with the cavitation hypothesis of Venet *et al.* (*17*), as the artery was not fully collapsed under the stethoscope and no cavitation bubbles were detected, whereas UUI is particularly sensitive to such events (*35*, *36*). The damped harmonic oscillator hypothesis (*21*, *22*) is also incompatible with our results, as it implies wall oscillations after artery dilation and compression. This second oscillation should be detected by ultrafast Doppler, which is sensitive to motion of ~3 μm. This mechanism does not explain either the KS frequency content. Third, the flow-related hypothesis (*18*, *19*) is also mostly opposed to our findings. We clearly showed that the blood flow was still very weak when the KS is perceived, with a typical delay in the range of ~40 ms between the KS and the maximum flow rate (Fig. 2, D to F). We can partially conciliate our results with previous ultrasound works on the topic (*23*–*25*). However, because of the constraints of conventional ultrasound imaging, the arterial wall could not be studied in space and time simultaneously. Hence, the propagative aspect of the problem was missed and so were the shear vibrations in tissues. These previous studies only established a synchronicity of KS with a strong motion at cuff outlet attributed to the arterial wall but could not directly explain the sound origin. Regarding the theory of the preanacrotic wave (*14*–*16*), we observed that the steepening and the shock of the pulse wave can create a short pressure dip, or breaker, known as the preanacrotic wave (Fig. 1D). Nevertheless, these forerunner wavelets have an insufficient amplitude and temporal extent to explain the full characteristics of the KS. They are more a side effect of the nonlinear propagation of the pulse wave (*42*). Last, Drzewiecki *et al.* (*20*) had already hypothesized the distortion of the pulse wave but did not explain the fundamental physical mechanisms. In particular, they used an empirical five-parameter law to describe the arterial pressure-area relationship and did not investigate how arterial motion was transmitted to the surrounding tissue, which is a key mechanism to explain why and when KSs are heard according to our results.

Are KSs really sound?

The results demonstrate that the KS source cannot be a sound wave but rather is a shear displacement induced in surrounding tissues and confined around the artery during the pulse wave propagation. As the pulse wave has a very different propagation speed (~1 to 5 m/s) compared to sound speed (1540 m/s), this alternative hypothesis explains the timing of the sound perception on the stethoscope and its localization. The originality of our study was to use UUI to track the transient and nonlinear propagation of the pulse wave both in space and time from the proximal to the distal edges of the cuff and to the stethoscope. Somehow ironically, McCutcheon *et al.* (*23*) were close to discovering this mechanism back in their 1971 work. They observed that the KSs were similar to the sound perceived in the stethoscope when briskly tapping the skin. They mistakenly concluded that KSs were "nonspecific." Tapping the skin creates shear waves within the tissue that are physically similar to the tissue shear displacements induced by the arterial pulse wave. The resulting sounds were comparable because they had the same physical mechanism.

The role of other waves

We can clearly see in Fig. 1, fig. S1, and movies S1 and S2 that the pulse wave is partially reflected as it exits the cuff because of the impedance difference between the compressed deformable segment of the artery under the cuff and the stretched, less deformable segment distal to the cuff. We observed that while most of the KS was perceived in the stethoscope before the reflection of the pulse wave occurred, the last sinusoid arches of the KS waveform corresponded to the reflected wave (fig S6). This suggests that, to a lesser extent, the reflected pulse wave also accounts for part of the KS spectral content.

In this work, we implicitly consider that the pulse wave at the origin of the KS is symmetrical around the longitudinal axis of the artery. It was recently evidenced that nonaxisymmetric pulse waves also propagate along the artery as flexural waves (*43*). These flexural pulse waves (FPWs) typically have a velocity one order of magnitude lower than the axisymmetric longitudinal pulse wave (LPW) and then may be incompatible with the observed timings. However, for low-transmural pressure, when the LPW velocity is considerably reduced, it may become comparable with the FPW velocity and then influence the KS. Nevertheless, we could confirm from our results that the upper wall and the lower wall had symmetrical velocity time courses when the KS was perceived. This is illustrated in fig. S6.

Perspectives for pressure measurements

Answering the question of KSs origins could have important clinical consequences. Even if the auscultatory method tends to be supplanted by automatic oscillometric assessment, the latter has well-

Downloaded from https://www.science.org on October 05, 2023

known limitations (*10*) that can lead to BP under/overestimation (*44*, *45*). KSs remain the calibration reference for these commercial devices with undisclosed algorithms, so understanding their mechanism is essential for BP measurements. In particular, accurately estimating DBP is challenging (*44*). Essentially, our findings show that the disappearance of the KS with decreasing cuff pressure is a gradual phenomenon. Not only the intensity of the KS decreases when the cuff pressure reaches the DBP, but we also showed that the frequency content of the KS is driven by the nonlinear propagation of the pulse wave. Hence, as shown in Fig 4A, around DBP, where the nonlinear behavior is less pronounced, the arterial wall velocity has a very low-pitched spectral content, in a range where the human ear has a very low sensitivity. This dependence of the frequency content with the propagation distance also explains why the position of the stethoscope can also influence the perception of the KS. All in all, the KS becomes fainter and deeper around DPB, which may explain why it is frequently overestimated, especially for hypertensive participants (*45*). We foresee that the curve of local PWV versus cuff pressure (Fig. 4E) might be used as a predictor of DBP, as it presents a sharp transition around DBP. Similarly, the curve of the shock distance versus cuff pressure also exhibits a sharp transition around DBP (Fig. 4D).

Perspectives and limitations of the theoretical model

A second major contribution of this work is to propose a physical model for KSs origins derived from the acoustoelasticity theory. Many of the current models for arterial pressure-area relationship implicitly rely on the linear elasticity theory. Here, to introduce the nonlinear framework of acoustoelasticity while keeping the model simple, we had to make several assumptions and choices.

First, we assumed that the arterial wall could be considered as an isotropic material to introduce the nonlinear Landau coefficients. This is a common assumption in works on wave propagation in arteries (*43*). It is well known however that arteries have anisotropic properties due the complex organization and properties of smooth muscles, elastin, and collagen fibers (*46*, *47*). Many studies proposed advanced constitutive modeling to account for these different constituents (*46*, *48*), which should be compared to the model proposed herein in subsequent works.

Second, we only considered the circumferential stretch of the artery. It would be more realistic to introduce also the axial and radial deformations. However, the theoretical derivation of the nonlinear PWV from the acoustoelasticity theory would become extremely complex and hardly interpretable in terms of physical properties. We would have to introduce nonlinear elastic Landau coefficients for all directions and would lose the easiness of interpretation of the theoretical equations relating the PWV to the transmural pressure and Landau coefficients and relating the shock distance with the material properties.

Third, we assumed an axisymmetric nature of the nonlinear problem. In particular, we considered that the vessel had a circular cross section throughout the problem. This axisymmetric assumption was found valid in our experiments, as seen for the example in fig. S6. However, it can be challenged at low transmural pressure levels ($\leq$0 mmHg), where the artery can collapse. In these cases, the simple Laplace law used to link the transmural pressure and the circumferential stress does not hold, and the fluid mechanics equations are not axisymmetric anymore. This nonaxisymmetric stress distribution could enhance the role of nonaxisymmetric modes such as the flexural waves described by Laloy-Borgna *et al.* (*43*). Similarly to Drzewiecki *et al.* (*29*), we considered that for transmural pressures above the buckling pressure (which is typically below 0 mmHg), the lumen area had a circular cross-sectional shape. It results that for the onset of the pulse wave, when the transmural pressure is very low, our model has intrinsic weaknesses but becomes more reliable as soon as the artery dilates under the rapidly rising BP.

These hypotheses were deemed necessary to allow the development of nonlinear elasticity theory within this complex biomechanical problem. We think that the final agreement between the shock distances estimated theoretically and experimentally shows at least the interest of this simplified model.

These results may open alternative ways to measure the mechanical properties of the artery. While many studies have shown links between PWV and arterial stiffness (*49*–*51*), they were unable to disentangle the concomitant effects of BP and structural properties of the arterial wall (*52*). Here, we demonstrated the impact of both intrinsic material parameters (arterial wall nonlinear elastic coefficients) and geometry (pressure-dependent arterial radius variations). We believe that our approach could lead to an innovative tool combining the auscultatory method and UUI able to study the intrinsic physical properties of the artery independently of the BP. In particular, noninvasive assessments of arterial stiffness may become possible and open up different perspectives for clinical practice.

MATERIALS AND METHODS

Definitions

Here, we define the transmural pressure as the difference between the BP in the collapsible segment of the artery and the sphygmomanometer cuff pressure. Hence, a negative transmural pressure means that the cuff pressure exceeds the arterial BP.

The longitudinal axis refers to the artery long axis. The term abscissa stands for the coordinate along the longitudinal axis. The radial axis is orthogonal to the artery long axis. The axial direction refers to the transducer main axis and corresponds to the depth axis.

Participant cohort

N = 15 healthy volunteers aged 24 to 32 years old were included in the study (ULTRAFASTECHO, NCT01096264) and gave informed consent. The protocol strictly complied with the ethical principles for medical research involving human participants of the World Medical Association Declaration of Helsinki. The data from the five first participants were used to improve the experimental setup and were not included in the results. Among the 10 remaining participants, only 6 were imaged with the probe at the three possible locations in the cuff.

Ultrasound sequences and preprocessing

All ultrasound data were collected with an ultrafast ultrasound research scanner (Aixplorer, SuperSonic Imagine, Aix-en-Provence, France). A hockey stick–shaped probe (SLH20-6, 192 elements, 0.14-mm pitch, 11.25 MHz; SuperSonic Imagine, Aix-en-Provence, France) was used for all the UUI acquisitions except SWE measurements. These were executed with a custom linear probe (128 elements, 0.2-mm pitch, 6.4 MHz; Vermon, Tours, France) using the system commercial SWE mode. UUI sequences consisted of

Downloaded from https://www.science.org on October 05, 2023

the emission and coherent compounding of nine plane waves (*53*), linearly tilted from −7.5° to +7.5°. The imaging depth was set to 30 mm. A pulse-repetition frequency of 10,800 Hz was used, yielding a frame rate of 1200 Hz. The total duration of the sequence was 400 ms. From the resulting IQ datasets, tissue signals and blood signals were separated using singular value decomposition (SVD) (*54*). The tissue and blood subspaces were adaptively determined using the spatial similarity matrix approach (*55*). Sequence programming and the postprocessing were done in MATLAB (The MathWorks, Natick, MA, USA).

Lagrangian tracking of arterial walls

Conceptually, IQ data are an Eulerian representation of the medium, each pixel describing a fixed spatial location along time. In this study, the arterial wall radial displacements typically reach several millimeters, whereas the pixel size in this direction is 137 μm. The Eulerian framework is then not ideal, as the arterial wall will move from one pixel to another along acquisition time. A Lagrangian approach was adopted to track the material points of the walls over time. We assumed that the arterial wall only experienced axial motions. Hence, the lateral position of the wall was considered constant. First, the Eulerian axial velocity field was computed using beamformed radio frequency cross-correlation (*56*) with cosine interpolation (*57*). $\mathbf{V_E}(z_E, x_E, t)$, with (z_E, x_E) being the constant spatial coordinates of the IQ pixels and t the frame index. Second, the positions of the upper and lower arterial walls were manually delineated on a given frame t_0 where they were clearly visible. For the upper wall, this initial Lagrangian coordinate is denoted by $z_L(x_E, t_0)$. Knowing the pixel size in the axial direction, it was possible to find the Eulerian coordinates $z_E^{\text{nearest}}(x_E, t_0)$ that is the closest to $z_L(x_E, t_0)$. The Lagrangian velocity $v_L(x_E, t_0)$ is then defined by Eq. 7, which can be considered a simple nearest neighbor approximation

$$v_L(x_E, t_0) = \mathbf{V_E}[z_E^{\text{nearest}}(x_E, t_0), x_E, t_0] \tag{7}$$

The Lagrangian coordinate of the wall at frame $t_0 + 1$ could then be computed using Eq. 8, with T being the time interval between two consecutive frames. By substituting $t_0 + 1$ to t_0 in these equations, the coordinate at $t_0 + 2$ can then be obtained, and so on. Similarly, the coordinates could be iteratively computed for $t < t_0$. Here, wall velocity implicitly refer to $v_L(x_E, t)$

$$z_L(x_E, t_0 + 1) = z_L(x_E, t_0) + v_L(x_E, t_0)\ T \tag{8}$$

More advanced interpolation or regularization techniques (*58*) can be used to improve the wall tracking but were deemed unnecessary given the relative simplicity of the arterial motion. See fig. 2A for an example. Note that because of the convention chosen for the depth axis orientation, negative velocities correspond to motion toward the probe.

Sphygmomanometer and stethoscope

A sphygmomanometer with a particular three-strap closure system was used (Vaquez-Laubry Classic, Spengler, Antony, France). The cuff was positioned with the opening directly over the brachial artery so that the probe could be inserted between the straps and image the vessel. The straps were tightened firmly to ensure a uniform transmission of the cuff pressure to the skin. SBP and DBP were measured with the cuff in this orientation and with the orientation suggested by the manufacturer (cuff opening on the other side of the arm). The values were in good accordance, with less than 5 mmHg of difference. An electronic pressure sensor (TBPDLNN005PGUCV, Honeywell, Charlotte, NC, USA) was mounted on the sphygmomanometer pipes to ensure a steady pressure level during ultrasound acquisitions. The KSs were recorded at the distal extremity of the cuff by inserting an electronic stethoscope (Littmann 3200M, 3M, Saint Paul, MN, USA) and using its extended frequency range mode (20 to 2000 Hz). The stethoscope signal was sampled at 4000 Hz and transmitted via Bluetooth to a host computer stethoscope (Littmann StethAssist software, 3M, Saint Paul, MN, USA).

Experimental protocol

The participants were in supine position, with the cuff at the level of their right atrium (*7*). We first measured their BP using the standard auscultatory method and defined a list of target pressure levels every 10 mmHg, starting at SBP + 10 mmHg, and decreasing to DBP − 10 mmHg. We then inserted the ultrasound probe and the stethoscope. We inflated the cuff at SBP + 30 mmHg and launched a 60-s stethoscope recording (the longest allowed by the manufacturer′s acquisition software). An in-house graphical user interface displayed the BP in real time on the scanner′s monitor, with the next target level highlighted. We slowly deflated the cuff until its pressure reached the target level. After the cuff pressure had remained stable for at least 3 s, the ultrasound sequence was allowed to start at the next cardiac cycle. After the acquisition, a few seconds were necessary for data transfer and save. Overall, it took around 15 to 20 s in total to reach the pressure target, stabilize the pressure, wait for the next cardiac cycle, and acquire and transfer the ultrasound data. Hence, only two to three acquisitions were done per 60-s-long stethoscope track. At the end of this 60-s period, the cuff was fully deflated to avoid venous congestion. After a few minutes, we then resumed the compression cycle and continued with the remaining pressure targets.

Synchronization

Ultrasound acquisitions were triggered by an ECG (AccuSync 42, Milford, CT, USA). A delay of 100 ms was programmed between the R wave and the ultrasound sequence start to account for the pulse wave propagation from the heart to the cuff. The ultrasound acquisition and the stethoscope recording were synchronized using a reference audio signal. At the start and the end of the ultrasound sequence, a trig signal was transmitted by the scanner to a signal generator (AFG3022C, Tektronix, Beaverton, OR, USA) programmed to emit a sinusoid at 400 Hz with 50 cycles, 2 Vpp, toward an earphone (CX 100, Sennheiser, Wedemark, Germany) taped to the stethoscope body. This resulted in two loud beeps audible in the stethoscope. After band-pass filtering of the stethoscope signal {[350 450] Hz, Butterworth filter order 5, zero-phase distortion using forward-backward filtering (*59*)}, these two audio markers were precisely located using NCC with a reference sinusoid. This extra signal adds no influence on the KS, whose PSD generally falls below −60 dB above 280 Hz (*31*). More detail regarding the synchronization of signals can be found in fig. S8 and Supplementary Text.

Downloaded from https://www.science.org on October 05, 2023

Cross-correlation in the audible range

To compare arterial wall velocities and stethoscope signal, we band-pass–filtered both signals in the range [20,250] Hz (Butterworth filter of order 5) to match with the stethoscope bandwidth and reject high-frequency noise. We compensated for the nonlinear phase-response of the Butterworth filter by using a zero-phase filtering function [forward-backward filtering, MATLAB function "filtfilt" (*59*)]. We made sure that both signals were filtered with the same frequency characteristics, without phase distortion, as otherwise, it may introduce strong artifacts in their comparison (*60*). We used NCC between the stethoscope signal and the filtered wall velocity to compare signal similarity and delay in Fig. 1 (MATLAB function xcorr). Signals were priorly centered and scaled by their SD. The NCC lag corresponding to the maximum NCC value was considered as the delay between the compared signals. The same NCC approach was also used to establish the time of arrival maps of Fig. 3.

Envelope comparison

Because of the constraints of the experimental protocol, we deflated the cuff every 60 s maximum. This constraint meant that the stethoscope, probe, and artery adopted slightly different relative positions from one compression cycle to the next. As a result, KS intensities could vary from one acquisition to the next simply because of these different configurations. Therefore, rather than comparing wall velocity and KSs individually, we took the longest stethoscope tracks available (60 s, each containing multiple KSs acquired at different cuff pressures, 14 tracks, $N = 6$ participants) and compared them in their entirety with the corresponding wall velocities, assuming that during these tracks, the setup configuration was constant. In this way, within a single track, we could fairly compare the sound intensity of multiple KSs by extracting their RMS envelope. The RMS envelope was computed on sliding temporal windows of 50 ms, roughly corresponding to the duration of a KS. The stethoscope recordings containing several KSs were normalized by their maximum and then compared against the corresponding normalized wall velocity RMS envelope. The tracks with a low signal-to-noise (SNR) ratio were excluded. The SNR was considered too low if the peak of the weakest KS was lower than 3 SDs of the audio background noise (fig. S9). This audio noise was mostly caused by friction of the stethoscope on the skin and the cuff.

Blood imaging

As mentioned earlier (see the "Ultrasound sequences and preprocessing" section), the blood signal is separated from the tissue signal using adaptive SVD filtering. The resulting blood IQ signal, denoted as $s^F(z, x, t)$, can be processed into Power Doppler (PD) and so-called pulsed wave Doppler (PWD). PD is the time integral of s^F envelope (Eq. 9) and is proportional to the concentration of red blood cell in a given pixel (Fig. 2D) (*61*)

$$PD(z,x) = \int |s^F(z,x,t)|^2 dt \tag{9}$$

PWD is the discrete short-time Fourier transform of $s^F(z, x, t)$ along the temporal dimension. For a given sample area, the resulting spectrogram (Fig. 2E) reflects the changes of blood axial velocity along time.

Spectral content

For each longitudinal abscissa, the PSD of the wall velocity was computed using Welch's overlapped segment averaging spectral estimation (*62*), with sliding windows of 300 ms and an 80% overlap. The PSD was then averaged between participants at each abscissa.

Experimental shock distance

Knowing the Lagrangian coordinates of the upper and lower arterial walls along time and assuming a cylindrical symmetry, we could derive the artery lumen area $A(x_E, t)$ at each abscissa x_E and along time. $\frac{dA}{dt}(x_E, t)$ surfaces were normalized by their maximum over the displayed time and space ranges. The characteristic curve at 20% is the intersection of the $\frac{dA}{dt}(x_E, t)$ surfaces with the horizontal plane of coordinates $(0.2, x_E, t)$. A least-square linear regression is fitted to the projection of each characteristic curve on the space/time horizontal plane. If the theoretical shock distance was lower than the probe width (17.9 mm), then only the part of the projected characteristic curves corresponding to spatial abscissas lower than this theoretical shock distance was used for linear regression. As the three fitted lines did not intersect exactly at the same point, the experimental shock distance was taken as the median spatial coordinates of the three intersection points.

Pulse wave velocity

The Lagrangian velocity $v_L(x_E, t)$ of the arterial upper wall can be visualized as a space-time image by considering all x_E and t coordinates (*63*). For each abscissa x_E, the pulse wave envelope was extracted using the Hilbert transform of $v_L(x_E, t)$ along time (*64*). The pulse wave envelope appears as a titled wavefront, whose slope is the pulse wave group velocity, in other words, the PWV. The normalized Radon transform of this space-time image was computed with angular increments of 0.1°. The angular direction that maximized the Radon transform was considered as orthogonal to the wavefront, and thus, the PWV could be computed (*65*).

Theory of pulse wave under cuff pressure: Equation of motion

The description of flow in elastic tubes as arterial vessels needs three independent variables namely the pressure $p(x, t)$, the fluid velocity $v(x, y)$ [or equivalently, the flow rate $Q(x, t)$], and the cross-sectional area $A(x, t)$. The main governing equations are the conservation of mass and momentum (i.e., the continuity and the momentum equations). In this problem, we only have two equations and three variables, namely, p, Q, and A. Therefore, we need a third relation that describes the deformation of the vessel walls due to a variation in the pressure. A third equation could be obtained from the energy conservation, which is related to the interaction between the fluid and the tube wall, or by analytical equations, which provide a relationship between the transmural (internal minus external) pressure p_{tm} and the variation in the cross-sectional area (or diameter), the so-called state equation or pressure-area $P - A$ constitutive relations.

The vessel is represented as a cylindrical tube (fig. S4) of length L, wall thickness h, inner (or internal) radius R_{int}, outer (or external) radius R_{ext}, and circular cross-sectional area $A(x, t) = \pi R^2$. Pressure-area equations provide relation between the transmural pressure p_{tm} and the variation in the cross-sectional area (or the radius). The transmural pressure is defined as $p_{tm} = p - p_{ext}$, where $p = p_{int}$ is

Downloaded from https://www.science.org on October 05, 2023

the internal fluid (blood) pressure and p_{ext} is the external pressure (from surrounding tissue). The variation in the area is between the tube section $A = \pi R^2$ (at internal fluid pressure p) and $A_0 = \pi {R_0}^2$ when there is zero transmural pressure (i.e., $p = p_{ext}$), where R_0 is the radius at $p_{tm} = 0$.

Navier-Stokes equations for an axisymmetric flow in a flexible tube can be derived. On the basis of the work of Comolet (*66*) and Lighthill (*67*), we may consider the governing equations for fluid flow without gravity or viscous term (*68*)

$$\begin{aligned} \partial_t A + \partial_x(Q) &= 0 \\ \partial_t Q &= -\tfrac{A}{\rho}\partial_x p \\ p &= K_p P(A) \end{aligned} \tag{10}$$

where ρ is the fluid density and K_p is a constant. The equations are linearized by considering small perturbations around the state $v = 0$, $A = A_0$, where A_0 is the reference area. Then

$$\begin{aligned} \partial_t A + \partial_x Q &= 0 \\ \partial_t Q &= -\tfrac{AK_p}{\rho}\tfrac{dP}{dA}\partial_x A \end{aligned} \tag{11}$$

Eliminating Q, one obtains the wave equation

$$\partial_{tt}^2 A - c^2 \partial_{xx}^2 A = 0 \tag{12}$$

where the speed of the pulse wave is given by

$$c^2 = \frac{AK_p}{\rho}\frac{dP}{dA} \tag{13}$$

A key question is then the pressure dependency with respect to the radius R or area A, which is highly dependent on the vessel viscoelastic properties.

Transmural pressure versus wall tension

Several approaches can be taken to write the relation between the pressure and the cross-sectional area. The arterial wall does not respond instantaneously to a change in pressure due to its viscoelastic behavior (*69*, *70*). However, these viscoelastic effects seem to be small within the physiological range of the flow and pressure (*71*). Therefore, many studies use relations derived from the linear theory of elasticity and disregard the viscoelastic behavior (*72*–*76*). In the following part, we will neglect viscosity effects. As the pressure load induced during the Korotkoff experiments is high and lead to major changes of elasticity, we will have to derive the $P - R$ relationship in the framework on nonlinear elasticity. In the following part, we will therefore build on the following assumptions: (i) The flow, loading, and deformation are axisymmetric. (ii) The arterial vessels walls are thin, i.e., $h \ll R$. (iii) The structural arterial properties are constant. (iv) The vessel is tethered in the longitudinal direction.

To obtain the relationship between the pressure and the cross-sectional area, we need first to examine the equilibrium of the internal and external forces acting on a unit element of the wall.

Pressure force

The elementary force due to the pressure differences is given by

$$dF_p = dF_{pint} - dF_{pext} = (p_{int}R_i - p_{ext}R_e)Ld\theta \tag{14}$$

For the half cylinder (fig. S4), the vertical component is

$$F_{p,1} = (p_{int}R_i - p_{ext}R_e)\ L\ sin(\theta)d\theta \tag{15}$$

After integrating from 0 to π, we obtain the vertical force due to the pressure differences

$$F_{p,1} = 2\ (p_{int}R_i - p_{ext}R_e)\ L \tag{16}$$

If the vessel is thin walled ($h \ll R$), then $R_i \approx R_e = R$ and

$$F_{p,1} = 2\ (p_{int} - p_{ext})\ R\ L = 2\ p_{tm}RL \tag{17}$$

Laplace's law

The aim is to link the transmural pressure to the tension in the walls related to the wall stress (force per unit area) σ. The force pulling the half cylinder down is

$$F_\sigma = 2\ \sigma hL \tag{18}$$

In equilibrium, F_σ is balanced by the vertical force due to the transmural pressure $F_{p,1}$ (Eq. 17)

$$\sigma h = p_{tm}R \tag{19}$$

$$p_{tm} = \frac{\sigma h}{R} \tag{20}$$

Equation 20 is an expression of Laplace's law for a thin-walled cylinder. Note that for a given transmural pressure, the wall tension ($T = \sigma h$) per unit length increases as the radius increases and vice versa.

Acoustoelasticity applied to $P - A$

Here, we propose to derive the theoretical $P - A$ relationship by taking into account the nonlinear elastic properties of the arterial wall (see Supplementary Text for considerations on the $P - A$ relationship under the linear elasticity framework). To better describe the propagation of the arterial pulse wave under a loading pressure p_{ext}, we have to introduce the acoustoelasticity theory describing the influence of stresses on the propagation of mechanical waves in nonlinear elastic solids. Many theoretical works have been devoted to the expression of the propagation velocity of elastic waves in a stretched nonlinear elastic soft solid (*41*, *77*, *78*) by revisiting the seminal work of Landau and Lifshitz (*40*).

Mechanics of a continuous medium

A disturbance in a medium is represented by a particle displacement with time-dependent position $u(x, t)$. The general equation of motion is given by

$$\rho\frac{\partial^2 u_i}{\partial t^2} = \frac{\partial \sigma_{ij}}{\partial x_j} \tag{21}$$

where ρ, σ_{ij}, and $\frac{\partial^2 u_i}{\partial t^2}$ designate the density, the second Piola-Kirchhoff stress tensor, and the particle acceleration, respectively. The Piola-Kirchhoff stress tensor is given by

$$\sigma_{ij} = \frac{\partial e}{\partial\left(\frac{\partial u_i}{\partial x_j}\right)} \tag{22}$$

with e, the strain energy density. In a general elastic medium, the strain energy density developed to the third order is

$$e = \frac{1}{2}C_{ijkl}\varepsilon_{ij}\varepsilon_{kl} + \frac{1}{6}C_{ijklmn}\varepsilon_{ij}\varepsilon_{kl}\varepsilon_{mn} \tag{23}$$

where C_{ijkl} and C_{ijklmn} designate the second- and third-order elastic

Downloaded from https://www.science.org on October 05, 2023

tensor, respectively and ε is the Lagrangian finite-strain tensor

$$\varepsilon_{ik} = \frac{1}{2}\left(\frac{\partial u_i}{\partial x_k} + \frac{\partial u_k}{\partial x_i} + \frac{\partial u_l}{\partial x_i}\frac{\partial u_l}{\partial x_k}\right) \quad (24)$$

also defined as the Lagrangian finite strain or Green-Lagrange strain tensor

$$E = \frac{1}{2}\ (F^{\mathrm{T}}F - I) \quad (25)$$

with $C = F^{\mathrm{T}}F$, being the right Cauchy-Green deformation tensor, which is commonly used in materials science. Therefore, E is a measure of how much C differs from identity I. Invariants of C are often used in the expressions for strain energy density functions. The most commonly used invariants are

$$\begin{aligned} I_1^C &= tr(\mathbf{C}) = \lambda_1^2 + \lambda_2^2 + \lambda_3^2 \\ I_2^C &= \tfrac{1}{2}\ [tr(\mathbf{C})^2 - tr(\mathbf{C}^2)] = \lambda_1^2\lambda_2^2 + \lambda_2^2\lambda_3^2 \\ I_3^C &= det(\mathbf{C}) = \lambda_1^2\lambda_2^2\lambda_3^2 \end{aligned} \quad (26)$$

Note that $I_3^C = 1$ for incompressible materials (see Supplementary Text for considerations on elastic tensors in linear regime).

Acoustoelasticity theory

Landau and Lifshitz (*40*) have established the general expression for the elastic energy density of an isotropic body in the fourth-order approximation introducing the third-order coefficients (A_L, B_L, C_L) and expressed in terms of invariants of Lagrangian (Green-Lagrange). From the components of a symmetrical tensor of rank two, we can form two quadratic scalar (ε_{ik}^2 and (ε_{ll}^2) and three cubic scalar (ε_{ll}^3, $\varepsilon_{ll}\varepsilon_{ik}^2$, and $\varepsilon_{ik}\varepsilon_{il}\varepsilon_{kl}$). Hence, the most general scalar containing terms quadratic and cubic in ε_{ik}, with scalar coefficient (since the body is isotropic) is

$$e = \mu\varepsilon_{ik}^2 + \frac{\lambda}{2}\varepsilon_{ll}^2 + \frac{1}{3}A_L\varepsilon_{ik}\varepsilon_{il}\varepsilon_{kl} + B_L\varepsilon_{ik}^2\varepsilon_{ll} + \frac{1}{3}C_L\varepsilon_{ll}^3 \quad (27)$$

and invariants defined as follows

$$\begin{aligned} I_1 &= tr(\mathbf{E}) \\ I_2 &= tr(\mathbf{E}^2) \\ I_3 &= tr(\mathbf{E}^3) \end{aligned} \quad (28)$$

The Lamé and the Landau coefficients as a function of the elastic moduli in the Voigt′s notations come from (*79*)

$$\lambda = c_{12}, \mu = c_{66}, A_L = 4c_{456}, B_L = c_{144}, C_L = c_{123}/2 \quad (29)$$

Hamilton *et al.* and Zabolotskaya *et al.* (*41*, *77*) also derived a fourth-order expansion of the elastic energy density of an isotropic medium separating effect due to compressibility and shear deformation. The motivation was to identify the terms and corresponding constants to describe nonlinear effects of shear deformation when effects of compressibility and coupling between shear and compressional waves are both negligible. They showed that P waves and S waves can be considered separately. The simplified strain energy density function for shear waves that relates the strain energy density of a material to the deformation gradient is

$$e = \mu I_2 + \frac{1}{3}A_L I_3 + D_L I_2^2 \quad (30)$$

with μ and A_L being the expansion of Landau and Lifshitz theory and the coefficient D_L identified as the fourth-order elastic constant. The Landau coefficient A_L determines the nonlinear shear stress (or behavior), while D_L is required to describe nonlinear distortion of shear mechanical waves in finite amplitudes (*41*). Last, Gennisson *et al.* (*78*) developed Eq. 21 to retrieve the shear wave speed when the material is subjected to a stress.

Stress field versus artery radius

To relate the arterial pulse wave speed to the area A, it is necessary to derive the stress field σ_{22} with respect to the radius R. Note that if we consider a tensile test with a stress applied in the direction 2, σ_{22}, with faces in axes 1 and 3 free to deform, then we can write the correct Cauchy-Green deformation tensor according to the incompressibility assumption

$$\boldsymbol{C} = \begin{pmatrix} \lambda_1^2 & 0 & 0 \\ 0 & \lambda_2^2 & 0 \\ 0 & 0 & \lambda_3^2 \end{pmatrix} = \begin{pmatrix} 1/\lambda & 0 & 0 \\ 0 & \lambda^2 & 0 \\ 0 & 0 & 1/\lambda \end{pmatrix} \quad (31)$$

with $\lambda = R/R_0$, with R_0 as the initial radius at zero stress, and R as the radius at stretch state. It comes that the Green-Lagrange strain tensor invariants in tension can be written as

$$\begin{aligned} I_1 &= tr(\mathbf{E}) = \tfrac{1}{2}\left(\lambda^2 + \tfrac{2}{\lambda} - 3\right) \\ I_2 &= tr(\mathbf{E}^2) = \tfrac{1}{4}\left[(\lambda^2 - 1)^2 + 2\left(\tfrac{1}{\lambda} - 1\right)^2\right] \\ I_3 &= tr(\mathbf{E}^3) = \tfrac{1}{8}\left[(\lambda^2 - 1)^3 + 2\left(\tfrac{1}{\lambda} - 1\right)^3\right] \end{aligned} \quad (32)$$

From Eq. 30, it comes that the strain energy density function can be written in tension as

$$\begin{aligned} e = \mu\ &\frac{1}{4}\left[(\lambda^2 - 1)^2 + 2\left(\frac{1}{\lambda} - 1\right)^2\right] \\ &+ \frac{A_L}{24}\left[(\lambda^2 - 1)^3 + 2\left(\frac{1}{\lambda} - 1\right)^3\right] \\ &+ \frac{D_L}{16}\left[(\lambda^2 - 1)^2 + 2\left(\frac{1}{\lambda} - 1\right)^2\right]^2 \end{aligned} \quad (33)$$

From the strain energy density function, using Eq. 22 and considering that $\sigma_{22} = \frac{\partial e}{\partial \lambda}$, we can express the stress as a function of λ

$$\begin{aligned} \sigma_{22} = \mu &\left[\lambda(\lambda^2 - 1) - \frac{1}{\lambda^2}\left(\frac{1}{\lambda} - 1\right)\right] \\ &+ \frac{A_L}{4}\left[\lambda(\lambda^2 - 1)^2 - \frac{1}{\lambda^2}\left(\frac{1}{\lambda} - 1\right)^2\right] \\ &+ \frac{D_L}{2}\left[(\lambda^2 - 1)^2 + 2\left(\frac{1}{\lambda} - 1\right)^2\right] \\ &\times \left[\lambda(\lambda^2 - 1) - \frac{1}{\lambda^2}\left(\frac{1}{\lambda} - 1\right)\right] \end{aligned} \quad (34)$$

Downloaded from https://www.science.org on October 05, 2023

After derivation, one obtains if $R/R_0 \gg 1$

$$\sigma_{22} = \mu\frac{R(R^2-R_0^2)}{R_0^2} + \left(\frac{A_L}{4} - \frac{3D_L}{2}\right)\frac{R(R^2-R_0^2)^2}{R_0^5} + \frac{D_L}{2}\frac{R(R^2-R_0^2)^3}{R_0^6} \quad (35)$$

By using the Laplace law (Eq. 20), we find the radius dependence of the transmural pressure

$$p_{tm} = \mu\frac{h}{{R_0}^3}(R^2-R_0^2) + \left(\frac{A_L}{4} - \frac{3D_L}{2}\right)\frac{h}{{R_0}^5}(R^2-R_0^2)^2 + \frac{D_L}{2}\frac{h}{{R_0}^7}(R^2-R_0^2)^3 \quad (36)$$

p_{tm} can be written with respect to tube area A

$$p_{tm} = \mu\frac{h}{\pi{R_0}^3}(A-A_0) + \left(\frac{A_L}{4} - \frac{3D_L}{2}\right)\frac{h}{\pi^2{R_0}^5}(A-A_0)^2 + \frac{D_L}{2}\frac{h}{\pi^3{R_0}^7}(A-A_0)^3 \quad (37)$$

Nonlinear pulse wave propagation: Derivation of propagation equation

Coming back to Eqs. 10 to 13 of axisymmetric flow in a flexible tube, we can now calculate the dp_{tm}/dA from Eq. 37

$$\frac{dp_{tm}}{dA} = \mu\frac{h}{\pi{R_0}^3} + 2\left(\frac{A_L}{4} - \frac{3D_L}{2}\right)\frac{h}{\pi^2{R_0}^5}(A-A_0) + 3\frac{D_L}{2}\frac{h}{\pi^3{R_0}^7}(A-A_0)^2 \quad (38)$$

Eliminating Q in the Eqs. 10 to 12, one obtains the arterial pulse wave equation

$$\partial_{tt}^2 A - \partial_x(c^2\partial_x A) = 0 \quad (39)$$

where the propagation speed c verifies

$$c^2 = \frac{AK_p}{\rho}\frac{dP}{dA} = \mu\frac{h}{\rho\pi{R_0}^3}A_0 + 2\left(\frac{A_L}{4} - \frac{3D_L}{2}\right)\frac{h}{\rho\pi^2{R_0}^5}(A-A_0)A_0 + 3\frac{D_L}{2}\frac{h}{\rho\pi^3{R_0}^7}A_0(A-A_0)^2 \quad (40)$$

Recalling that $A_0 = \pi{R_0}^2$, we introduce the speed in the absence of nonlinear elasticity and in the absence of arterial pulse wave under the cuff

$${c_0}^2 = \frac{h\mu(p_{cuff})}{\rho R_0} \quad (41)$$

where $\mu(p_{cuff})$ should be considered as the shear modulus of the vessel under constraint but in the absence of pulse wave (and not the shear modulus at zero stress). This speed corresponds roughly to the Moens-Korteweg equation

$$c_0 = \sqrt{\frac{Eh}{3\rho R_0}} \quad (42)$$

where E is the Young's modulus of the artery under the cuff and $E \approx 3\mu(p_{cuff})$. If one keeps the nonlinear terms

$$c^2 = \frac{A_0}{\rho}\left[\mu\frac{h}{\pi{R_0}^3} + \left(\frac{A_L}{4} - \frac{3D_L}{2}\right)\frac{2h}{\pi^2{R_0}^5}(A-A_0) + \frac{3D_L}{2}\frac{h}{\pi^3{R_0}^7}(A-A_0)^2\right] \quad (43)$$

with $A_0 = \pi{R_0}^2$, the propagation equation can be written

$$\partial_{tt}^2 A - \partial_x\left\{\left[\mu\frac{h}{\rho R_0} + \left(\frac{A_L}{4} - \frac{3D_L}{2}\right)\frac{2h}{\rho\pi{R_0}^3}(A-A_0) + \frac{3D_L}{2}\frac{h}{\rho\pi^2{R_0}^5}(A-A_0)^2\right]\partial_x A\right\} = 0 \quad (44)$$

This nonlinear equation can be factorized into two counter-propagating terms:

$$\left[\partial_t A - c_0\partial_x A - \left(\frac{A_L}{4} - \frac{3D_L}{2}\right)\frac{h}{\rho c_0\pi{R_0}^3}(A-A_0)\partial_x A - \frac{3D_L}{4}\frac{h}{\rho c_0\pi^2{R_0}^5}(A-A_0)^2\partial_x A\right]$$
$$\left[\partial_t A + c_0\partial_x A + \left(\frac{A_L}{4} - \frac{3D_L}{2}\right)\frac{h}{\rho c_0\pi{R_0}^3}(A-A_0)\partial_x A + \frac{3D_L}{4}\frac{h}{\rho c_0\pi^2{R_0}^5}(A-A_0)^2\partial_x A\right] = 0 \quad (45)$$

If we keep only the term propagating toward the increasing x values, we obtain

$$\partial_t A - c_0\partial_x A - \left(\frac{A_L}{4} - \frac{3D_L}{2}\right)\frac{h}{\rho c_0\pi{R_0}^3}(A-A_0)\partial_x A - \frac{3D_L}{4}\frac{h}{\rho c_0\pi^2{R_0}^5}(A-A_0)^2\partial_x A = 0 \quad (46)$$

or

$$\partial_t A - c_0\partial_x A - \left(\frac{A_L}{4} - \frac{3D_L}{2}\right)\frac{c_0}{\mu\pi{R_0}^2}(A-A_0)\partial_x A - \frac{3D_L}{4}\frac{c_0}{\mu\pi^2{R_0}^4}(A-A_0)^2\partial_x A = 0 \quad (47)$$

Last, we obtain the nonlinear wave equation for the propagation of the arterial pulse wave under the cuff given by

$$\partial_t A - \left[c_0 + \left(\frac{A_L}{4} - \frac{3D_L}{2}\right)\frac{c_0}{\mu\pi{R_0}^2}(A-A_0) + \frac{3D_L}{4}\frac{c_0}{\mu\pi^2{R_0}^4}(A-A_0)^2\right]\partial_x A = 0 \quad (48)$$

This equation can be seen as a Burgers equation for the propagation of the pulse wave under the cuff. We see that the propagation

Downloaded from https://www.science.org on October 05, 2023

speed depends on the local radius

$$c = c_0 + \left(\frac{A_L}{4} - \frac{3D_L}{2}\right)\frac{c_0}{\mu {R_0}^2}(R^2 - {R_0}^2) + \frac{3D_L}{4}\frac{c_0}{\mu {R_0}^4}(R^2 - {R_0}^2)^2 \tag{49}$$

During the propagation of the pulse wave under the cuff, the high values of BP induce a larger arterial radius and result in a faster propagation than the lower values of BP, inducing a smaller arterial radius. If the nonlinear elastic coefficients are non-negligible compared to the linear elastic properties, then it results in a highly nonlinear propagation and a progressive and cumulative distortion of the arterial wall motion during the propagation under the cuff.

Derivation of the shock distance

To estimate the shock distance, we have to introduce the characteristics method. The aim of the characteristic curve method is to transform the governing partial differential equation into a set of coupled ordinary differential equations along certain curves known as characteristic curves or simply characteristics along the propagation axis.

Instead of solving the equation on the surface (x, t), we look for spatial curves on which the partial differential equation is reduced to set of ordinary differential equations along these curves. We choose an arbitrary 1D curve [$t(s)$, $x(s)$] and want to determine $A(s)$, where s is a parameter that increases along the curve.

We apply the method of characteristics using Eq. 48 to convert the initial value problem

$$\partial_t A - \left[c_0 + 2\left(\frac{A_L}{4} - \frac{3D_L}{2}\right)\frac{c_0}{\mu\pi {R_0}^2}(A - A_0) + \frac{3D_L}{2}\frac{c_0}{\mu\pi^2 {R_0}^4}(A - A_0)^2\right]\partial_x A = 0 \tag{50}$$

or

$$\partial_t A - F(A)\partial_x A = 0 \tag{51}$$

with the initial condition

$$A(x, 0) = A_0(x) \tag{52}$$

into the following two fully coupled characteristic ordinary differential equations

$$\begin{cases} \frac{dx}{dt} = F[A(x(t), t] & x(0) = \xi \\ \frac{dA}{dt} = 0 & A(\xi, 0) = A_0 \end{cases} \tag{53}$$

Since $dA/dt = 0$ and $A = A_0$, the characteristic curves $dx/dt = F(A_0)$ are straight lines. We can obtain the equation of a particular characteristic curve $x = x(t)$ in the (x, t) plane from the former equation as follows

$$\frac{dx}{dt} = F[A(x, t)] = F[A(\xi, 0)] = F[A_0(\xi)] \tag{54}$$

Direct integration gives the characteristic curve $x = x(t)$ as follows

$$x = \xi + F[A_0(\xi)].t \tag{55}$$

where ξ is the x intercept of the characteristic line. This equation shows that the characteristics are lines in (x, t) plane emanating from (ξ,0) with slope $\frac{1}{F[A_0(\xi)]}$. See Fig. 4 (B and C) for examples.

For some smooth initial waveform A_0, characteristic curves may intersect at a critical time t_s. Thus, the point (x_s, t_s) lies on two characteristics with different values of ξ and, hence, different values of A. The result of this is that the solution A for $t > t_s$ becomes multivalued. To define a solution for the partial differential equation after this critical time, we need to allow discontinuities in A. These discontinuities are known as shocks. At this point, we can define the shock distance $x_s = L_s$. Let us now derive a detailed description of the shock theory, how they are formed, and how to locate them.

The breaking time is the minimum time at which the first intersection of characteristics occurs. Suppose two characteristics emanate initially from the points ξ_1 and $\xi_2 = \xi_1 + \Delta\xi$. For $t \geq 0$, these characteristics will intersect when

$$\xi_1 + F(A_0)(\xi_1)t = \xi_2 + F(A_0)(\xi_2)t \tag{56}$$

To find the shock distance, we can take $\xi_1 = 0$, $\xi_2 = \lambda_{pw}/2$, with λ_{pw} the wavelength of the pulse wave. We search when the higher radius R_{max} will overtake the minimal radius R_0 during propagation.

This shock distance L_s is reached when the smaller radius R_d (for diastole) has traveled during a distance r_d where the discontinuity appears, with a velocity c_d. This discontinuity appears at time t_s

$$r_d = \left[c_0 + \left(\frac{A_L}{4} - \frac{3D_L}{2}\right)\frac{c_0}{\mu\pi {R_0}^2}({R_d}^2 - {R_0}^2) + \frac{3D_L}{4}\frac{c_0}{\mu\pi^2 {R_0}^4}({R_d}^2 - {R_0}^2)^2\right] \times \frac{L_S}{c_d} \tag{57}$$

At this breaking time t_s, the maximum radius has traveled a distance r_s

$$r_s = \left[c_0 + \left(\frac{A_L}{4} - \frac{3D_L}{2}\right)\frac{c_0}{\mu\pi {R_0}^2}({R_{max}}^2 - {R_0}^2) + \frac{3D_L}{4}\frac{c_0}{\mu\pi^2 {R_0}^4}({R_{max}}^2 - {R_0}^2)^2\right] t_s \tag{58}$$

The shock is reached when $r_d - r_s$ corresponds to the half wavelength $\lambda_{pw}/2$ of the arterial pulse wave under the cuff, meaning $r_d - L_s = \lambda_{pw}/2$

$$r_d - L_S = \left\{\left(\frac{A_L}{4} - \frac{3D_L}{2}\right)\frac{c_0}{\mu\pi {R_0}^2}({R_{max}}^2 - {R_d}^2) + \frac{3D_L}{4}\frac{c_0}{\mu\pi^2 {R_0}^4}[({R_{max}}^2 - {R_0}^2)^2 - ({R_d}^2 - {R_0}^2)^2]\right\}\frac{L_S}{c_d} = \frac{\lambda_{pw}}{2} \tag{59}$$

$$r_d - L_S = \left[\left(\frac{A_L}{4} - \frac{3D_L}{2}\right)\frac{c_0}{\mu\pi {R_0}^2}({R_{max}}^2 - {R_d}^2) + \frac{3D_L}{4}\frac{c_0}{\mu\pi^2 {R_0}^4}({R_{max}}^2 - {R_d}^2)({R_{max}}^2 + {R_d}^2 - 2{R_0}^2)\right]\frac{L_S}{c_d} = \frac{\lambda_{pw}}{2} \tag{60}$$

$$r_d - L_S \approx \left[\left(\frac{A_L}{4} - \frac{3D_L}{2}\right)\frac{c_0}{\mu\pi {R_0}^2}({R_{max}}^2 - {R_d}^2) + \frac{3D_L}{4}\frac{c_0}{\mu\pi^2 {R_0}^4}({R_{max}}^4 - {R_d}^4)\right]\frac{L_S}{c_d} = \frac{\lambda_{pw}}{2} \tag{61}$$

Downloaded from https://www.science.org on October 05, 2023

Thus, we obtain the shock distance

$$L_S = \frac{\lambda_{pw}\mu\pi {R_0}^2}{\left(\frac{A_L}{2} - 3D_L\right)\left({R_{max}}^2 - {R_d}^2\right) + \frac{3D_L}{4\pi {R_0}^2}\left({R_{max}}^4 - {R_d}^4\right)} \frac{c_d}{c_0} \quad (62)$$

$$L_S = \frac{\lambda_{pw}\mu\pi {R_0}^2}{\left(\frac{A_L}{2} - 3D_L\right)\left({R_{max}}^2 - {R_d}^2\right) + \frac{3D_L}{4\pi {R_0}^2}\left({R_{max}}^4 - {R_d}^4\right)} \left(1 + \frac{{R_d}^2 - {R_0}^2}{{R_0}^2}\right) \quad (63)$$

or

$$L_S = \frac{\lambda_{pw}}{\pi} \cdot \frac{\mu\pi {R_d}^2}{\left(\frac{A_L}{2} - 3D_L\right)\left({R_{max}}^2 - {R_d}^2\right) + \frac{3D_L}{4\pi {R_0}^2}\left({R_{max}}^4 - {R_d}^4\right)} \quad (64)$$

or

$$L_S = \lambda_{pw} \cdot \frac{\mu\pi}{\left(\frac{A_L}{2} - 3D_L\right) + \frac{3D_L}{4\pi {R_0}^2}\left({R_{max}}^2 + {R_d}^2\right)} \cdot \frac{{R_d}^2}{R_{max}^2 - {R_d}^2} \quad (65)$$

When the nonlinear term $\frac{3D_L}{4\pi {R_0}^2}\left({R_{max}}^2 + {R_d}^2\right)$ is considered negligeable compared to $\left(\frac{A_L}{2} - 3D_L\right)$, the shock distance L_s can be finally simplified in first approximation to

$$L_S = \lambda_{pw} \cdot \frac{\mu\pi}{\left(\frac{A_L}{2} - 3D_L\right)} \cdot \frac{{R_d}^2}{R_{max}^2 - {R_d}^2} \quad (66)$$

We see that the shock distance directly depends on the ratio between the linear elastic coefficient $\mu(p_{diast} - p_{cuff})$ under the cuff during diastole (i.e., before the pulse wave attains the cuff) and the nonlinear elastic parameters at maximal distortion during the pulse wave propagation multiplied by the squared ratio between the minimal and maximal radius

$$L_S = \lambda_{pw} \cdot \frac{\pi\mu(p_{cuff} - p_{diast})}{\frac{A_L}{2} - 3D_L} \cdot \frac{{R_d}^2}{R_{max}^2 - {R_d}^2} \quad (67)$$

λ_{pw} is the wavelength of the pulse wave under the cuff, corresponding approximately to

$$\lambda_{pw} = \frac{1}{f_0}\sqrt{\frac{\mu(p_{syst} - p_{cuff})}{\rho}} \quad (68)$$

where f_0 is the central frequency of the pulse wave signal and ρ is the density.

Calculation of the shock distance

Equation 67 can be simplified by introducing the ratio $\boldsymbol{\gamma}$ of the linear and nonlinear elastic coefficients

$$\boldsymbol{\gamma} = \frac{\pi\mu}{\frac{A_L}{2} - 3D_L} \quad (69)$$

$$L_S = \lambda_{pw}\, \boldsymbol{\gamma}\, \frac{{R_d}^2}{R_{max}^2 - {R_d}^2} \quad (70)$$

The nonlinear Landau coefficients of arteries A_L and D_L are unknown to date in the literature. To derive a typical value for $\boldsymbol{\gamma}$, we fitted our $P - A$ relationship (Eq. 37) to published experimental $P - A$ curves. After least-square fitting, we could estimate $\boldsymbol{\gamma}$ by doing the ratio of the first- and second-order terms of the fitted expression that is equal to $2R_0^2\boldsymbol{\gamma}$. The results of Fig. 4 and fig. S5 were obtained using the curve from Drzewiecki *et al.* (*29*) on excised canine carotid artery, giving $\boldsymbol{\gamma}$ = 2.26. We also considered noninvasive measurements in human brachial arteries from Drzewiecki and Pilla (*80*) and Bank *et al.* (*81*), giving respectively 1.90 and 1.96 for $\boldsymbol{\gamma}$. These experimental $P - A$ curves are reproduced in fig. S11 along with the fitted curves. The three theoretical shock distance curves corresponding to these three values of $\boldsymbol{\gamma}$ are also reported in fig. S11, with no major differences.

Supplementary Materials

This PDF file includes:

Supplementary Text
Figs. S1 to S11
Table S1
Legends for movies S1 to S4
References

Other Supplementary Material for this manuscript includes the following:

Movies S1 to S4

REFERENCES AND NOTES

1. P. M. Kearney, M. Whelton, K. Reynolds, P. K. Whelton, J. He, Worldwide prevalence of hypertension. *J. Hypertens.* **22**, 11–19 (2004).
2. D. Ettehad, C. A. Emdin, A. Kiran, S. G. Anderson, T. Callender, J. Emberson, J. Chalmers, A. Rodgers, K. Rahimi, Blood pressure lowering for prevention of cardiovascular disease and death: A systematic review and meta-analysis. *Lancet* **387**, 957–967 (2016).
3. NCD Risk Factor Collaboration (NCD-RisC), Worldwide trends in hypertension prevalence and progress in treatment and control from 1990 to 2019: A pooled analysis of 1201 population-representative studies with 104 million participants. *Lancet* **398**, 957–980 (2021).
4. M. Brunström, B. Carlberg, Association of blood pressure lowering with mortality and cardiovascular disease across blood pressure levels. *JAMA Intern. Med.* **178**, 28–36 (2018).
5. B. Williams, G. Mancia, W. Spiering, E. A. Rosei, M. Azizi, M. Burnier, D. L. Clement, A. Coca, G. de Simone, A. Dominiczak, T. Kahan, F. Mahfoud, J. Redon, L. Ruilope, A. Zanchetti, M. Kerins, S. E. Kjeldsen, R. Kreutz, S. Laurent, G. Y. H. Lip, R. McManus, K. Narkiewicz, F. Ruschitzka, R. E. Schmieder, E. Shlyakhto, C. Tsioufis, V. Aboyans, I. Desormais; ESC Scientific Document Group, 2018 ESC/ESH guidelines for the management of arterial hypertension. *Eur. Heart J.* **39**, 3021–3104 (2018).
6. E. O'Brien, D. Fitzgerald, The history of blood pressure measurement. *J. Hum. Hypertens.* **8**, 73–84 (1994).
7. P. Muntner, D. Shimbo, R. M. Carey, J. B. Charleston, T. Gaillard, S. Misra, M. G. Myers, G. Ogedegbe, J. E. Schwartz, R. R. Townsend, E. M. Urbina, A. J. Viera, W. B. White, J. T. Wright Jr., Measurement of blood pressure in humans: A scientific statement from the American Heart Association. *Hypertension* **73**, e35–e66 (2019).
8. B. S. Alpert, D. Quinn, D. Gallick, Oscillometric blood pressure: A review for clinicians. *J. Am. Soc. Hypertens.* **8**, 930–938 (2014).
9. T. M. Kazamias, M. P. Gander, D. L. Franklin, J. Ross Jr., Blood pressure measurement with Doppler ultrasonic flowmeter. *J. Appl. Physiol.* **30**, 585–588 (1971).
10. A. Benmira, A. Perez-Martin, I. Schuster, I. Aichoun, S. Coudray, F. Bereksi-Reguig, M. Dauzat, From Korotkoff and Marey to automatic non-invasive oscillometric blood pressure measurement: Does easiness come with reliability? *Expert Rev. Med. Devices* **13**, 179–189 (2016).
11. A. S. Vischer, T. Burkard, "Principles of blood pressure measurement—Current techniques, office vs ambulatory blood pressure measurement." in *Hypertension: From Basic Research to Clinical Practice*, Md. S. Islam, Ed. (Springer International Publishing, 2017), pp. 85–96.
12. C. E. Grim, C. M. Grim, Auscultatory BP: Still the gold standard. *J. Am. Soc. Hypertens.* **10**, 191–193 (2016).
13. J. Erlanger, Studies in blood pressure estimations by indirect methods. *Am. J. Physiol.* **39**, 401–446 (1916).
14. J. Erlanger, The relation of longitudinal tension of an artery to the preanacrotic (breaker) phenomenon. *Am. Heart J.* **19**, 398–400 (1940).

Downloaded from https://www.science.org on October 05, 2023

15. C. Bramwell, The arterial pulse in health and disease. *Lancet* **230**, 366–371 (1937).
16. M. E. Tavel, J. Faris, W. K. Nasser, H. Feigenbaum, C. Fisch, Korotkoff sounds. Observations on pressure-pulse changes underlying their formation. *Circulation* **39**, 465–474 (1969).
17. R. Venet, D. Miric, A. Pavie, D. Lacheheb, Korotkoff sound: The cavitation hypothesis. *Med. Hypotheses* **55**, 141–146 (2000).
18. S. Rodbard, The significance of the intermediate Korotkoff sounds. *Circulation* **8**, 600–604 (1953).
19. R. L. Lange, R. P. Carlisle, H. H. Hecht, Observations on vascular sounds: The "Pistol-Shot" sound and the Korotkoff sound. *Circulation* **13**, 873–883 (1956).
20. G. M. Drzewiecki, J. Melbin, A. Noordergraaf, The Krotkoff sound. *Ann. Biomed. Eng.* **17**, 325–359 (1989).
21. M. Anliker, K. R. Raman, Korotkoff sounds at diastole—A phenomenon of dynamic instability of fluid-filled shells. *Inter J. Solid Struct.* **2**, 467–472 (1966).
22. C. F. Babbs, The origin of Korotkoff sounds and the accuracy of auscultatory blood pressure measurements. *J. Am. Soc. Hypertens.* **1**–**16**, 935–50.e3 (2015).
23. E. P. McCutcheon, R. F. Rushmer, O. Jacobson, H. Sandier, Korotkoff sounds. *Circ. Res.* **20**, 149–161 (1967).
24. D. A. Sykes, K. McCarty, E. Mulkerrin, D. J. Fisher, J. P. Woodcock, Correlation between Korotkoff's sounds and ultrasonics of the brachial artery in healthy and normotensive subjects. *Clin. Phys. Physiol. Meas.* **12**, 327–331 (1991).
25. A. Benmira, A. Perez-Martin, I. Schuster, F. Veye, J. Triboulet, N. Berron, I. Aichoun, S. Coudray, J. Laurent, F. Bereksi-Reguig, M. Dauzat, An ultrasound look at Korotkoff sounds. *Blood Press. Monit.* **22**, 86–94 (2017).
26. G. Parati, J. E. Ochoa, C. Lombardi, G. Bilo, Assessment and management of blood-pressure variability. *Nat. Rev. Cardiol.* **10**, 143–155 (2013).
27. M. Tanter, M. Fink, Ultrafast imaging in biomedical ultrasound. *IEEE Trans. Ultrason. Ferroelectr. Freq. Control* **61**, 102–119 (2014).
28. P. Segers, E. R. Rietzschel, J. A. Chirinos, How to measure arterial stiffness in humans. *Arterioscler. Thromb. Vasc. Biol.* **40**, 1034–1043 (2020).
29. G. Drzewiecki, S. Field, I. Moubarak, J. K.-J. Li, Vessel growth and collapsible pressure-area relationship. *American J Physiol-Heart Circ Physiol* **273**, H2030–H2043 (1997).
30. D. L. Newman, N. J. Masters, J. F. McNulty, Pulse-wave reflection in elastic tubes. *Med. Biol. Eng.* **13**, 720–726 (1975).
31. J. Allen, T. Gehrke, J. J. O'Sullivan, S. T. King, A. Murray, Characterization of the Korotkoff sounds using joint time-frequency analysis. *Physiol. Meas.* **25**, 107–117 (2004).
32. L. J. Nowak, K. M. Nowak, An experimental study on the role and function of the diaphragm in modern acoustic stethoscopes. *Appl. Acoust.* **155**, 24–31 (2019).
33. A. J. Zuckerwar, Acoustical measurement, in *Encyclopedia of Physical Science and Technology* (Elsevier Science, 2003).
34. F. Pan, F. Chen, C. Liu, Z. Yang, Z. Liu, D. Zheng, Quantitative comparison of Korotkoff sound waveform characteristics: Effects of static cuff pressures and stethoscope positions. *Ann. Biomed. Eng.* **46**, 1736–1744 (2018).
35. B. Arnal, J. Baranger, C. Demene, M. Tanter, M. Pernot, In vivo real-time cavitation imaging in moving organs. *Phys. Med. Biol.* **62**, 843–857 (2017).
36. J. Gateau, J. F. Aubry, M. Pernot, M. Fink, M. Tanter, Combined passive detection and ultrafast active imaging of cavitation events induced by short pulses of high-intensity ultrasound. *IEEE Trans. Ultrason. Ferroelectr. Freq. Control* **58**, 517–532 (2011).
37. J. Mamou, M. L. Oelze, *Quantitative Ultrasound in Soft Tissues* (Springer, 2013).
38. J. Bercoff, M. Tanter, M. Fink, Supersonic shear imaging: A new technique for soft tissue elasticity mapping. *IEEE Trans. Ultrason. Ferroelectr. Freq. Control* **51**, 396–409 (2004).
39. E. G. Earl, G. Williams, *Fourier Acoustics: Sound Radiation and Nearfield Acoustical Holography* (Academic Press, 1999).
40. L. D. Lev, D. Landau, E. M. Evgeniĭ, M. Lifshitz, A. Markovich Kosevich, L. P. Lev, P Pitaevskiĭ, *Theory of Elasticity* (Butterworth-Heinemann, 1986).
41. M. F. Hamilton, Y. A. Ilinskii, E. A. Zabolotskaya, Separation of compressibility and shear deformation in the elastic energy density (L). *J. Acoust. Soc. Am.* **116**, 41–44 (2004).
42. P. Flaud, D. Geiger, C. Oddou, High amplitude wave propagation in collapsible tubes. II. Forerunners and high amplitude waves. *J de Physique.* **47**, 773–780 (1986).
43. G. Laloy-Borgna, L. Puyo, H. Nishino, M. Atlan, S. Catheline, Observation of natural flexural pulse waves in retinal and carotid arteries for wall elasticity estimation. *Sci Adv* **9**, eadf1783 (2023).
44. T. R. Holt, D. E. Withington, E. Mitchell, Which pressure to believe? A comparison of direct arterial with indirect blood pressure measurement techniques in the pediatric intensive care unit. *Pediatr. Crit. Care Med.* **12**, 391–394 (2011).
45. D. S. Picone, M. G. Schultz, P. Otahal, S. Aakhus, A. M. Al-Jumaily, J. A. Black, W. J. Bos, J. B. Chambers, C.-H. Chen, H.-M. Cheng, A. Cremer, J. E. Davies, N. Dwyer, B. A. Gould, A. D. Hughes, P. S. Lacy, E. Laugesen, F. Liang, R. Melamed, S. Muecke, N. Ohte, S. Okada, S. Omboni, C. Ott, X. Peng, T. Pereira, G. Pucci, R. Rajani, P. Roberts-Thomson, N. B. Rossen, D. Sueta, M. D. Sinha, R. E. Schmieder, H. Smulyan, V. K. Srikanth, R. Stewart, G. A. Stouffer, K. Takazawa, J. Wang, B. E. Westerhof, F. Weber, T. Weber, B. Williams, H. Yamada, E. Yamamoto, J. E. Sharman, Accuracy of cuff-measured blood pressure. *J. Am. Coll. Cardiol.* **70**, 572–586 (2017).
46. K. D. Reesink, B. Spronck, Constitutive interpretation of arterial stiffness in clinical studies: A methodological review. *J Physiol-Heart Circul Physiol* **316**, H693–H709 (2019).
47. J. Ferruzzi, M. R. Bersi, J. D. Humphrey, Biomechanical phenotyping of central arteries in health and disease: Advantages of and methods for murine models. *Ann. Biomed. Eng.* **41**, 1311–1330 (2013).
48. B. Spronck, M. H. G. Heusinkveld, W. P. Donders, A. G. W. De Lepper, J. O. Roodt, A. A. Kroon, T. Delhaas, K. D. Reesink, A constitutive modeling interpretation of the relationship among carotid artery stiffness, blood pressure, and age in hypertensive subjects. *J Physiol-Heart Circul Physiol* **308**, H568–H582 (2015).
49. J. Sugawara, K. Hayashi, T. Yokoi, M. Y. Cortez-Cooper, A. E. DeVan, M. A. Anton, H. Tanaka, Brachial-ankle pulse wave velocity: An index of central arterial stiffness? *J. Hum. Hypertens.* **19**, 401–406 (2005).
50. G. Goudot, C. Papadacci, B. Dizier, V. Baudrie, I. Ferreira, C. Boisson-Vidal, M. Tanter, X. Jeunemaître, M. Pernot, E. Messas, T. Mirault, Arterial stiffening with ultrafast ultrasound imaging gives new insight into arterial phenotype of vascular Ehlers-Danlos mouse models. *Ultraschall Med* **40**, 734–742 (2019).
51. T. Mirault, M. Pernot, M. Frank, M. Couade, R. Niarra, M. Azizi, J. Emmerich, X. Jeunemaître, M. Fink, M. Tanter, E. Messas, Carotid stiffness change over the cardiac cycle by ultrafast ultrasound imaging in healthy volunteers and vascular Ehlers-Danlos syndrome. *J. Hypertens.* **33**, 1890–1896 (2015).
52. B. Spronck, M. H. G. Heusinkveld, F. H. Vanmolkot, J. O. Roodt, E. Hermeling, T. Delhaas, A. A. Kroon, K. D. Reesink, Pressure-dependence of arterial stiffness. *J. Hypertens.* **33**, 330–338 (2015).
53. G. Montaldo, M. Tanter, J. Bercoff, N. Benech, M. Fink, Coherent plane-wave compounding for very high frame rate ultrasonography and transient elastography. *IEEE Trans. Ultrason. Ferroelectr. Freq. Control* **56**, 489–506 (2009).
54. C. Demene, T. Deffieux, M. Pernot, B.-F. Osmanski, V. Biran, J.-L. Gennisson, L.-A. Sieu, A. Bergel, S. Franqui, J.-M. Correas, I. Cohen, O. Baud, M. Tanter, Spatiotemporal clutter filtering of ultrafast ultrasound data highly increases Doppler and ultrasound sensitivity. *IEEE Trans. Med. Imaging* **34**, 2271–2285 (2015).
55. J. Baranger, B. Arnal, F. Perren, O. Baud, M. Tanter, C. Demené, Adaptive spatiotemporal SVD clutter filtering for ultrafast Doppler imaging using similarity of spatial singular vectors. *IEEE Trans. Med. Imaging* **37**, 1574–1586 (2018).
56. E. E. Jianwen Luo, A fast normalized cross-correlation calculation method for motion estimation. *IEEE Trans. Ultrason. Ferroelectr. Freq. Control* **57**, 1347–1357 (2010).
57. P. Dejong, T. Arts, A. Hoeks, R. Reneman, Determination of tissue motion velocity by correlation interpolation of pulsed ultrasonic echo signals. *Ultrason. Imaging* **12**, 84–98 (1990).
58. P. Cormier, J. Poree, C. Bourquin, J. Provost, Dynamic myocardial ultrasound localization angiography. *IEEE Trans. Med. Imaging* **40**, 3379–3388 (2021).
59. F. Gustafsson, Determining the initial states in forward-backward filtering. *IEEE Transactions on Signal Processing.* **44**, 988–992 (1996).
60. A. P. G. Hoeks, J. M. Willigers, R. S. Reneman, Effects of assessment and processing techniques on the shape of arterial pressure-distension loops. *J. Vasc. Res.* **37**, 494–500 (2000).
61. J. M. Rubin, R. O. Bude, P. L. Carson, R. L. Bree, R. S. Adler, Power Doppler US: A potentially useful alternative to mean frequency-based color Doppler US. *Radiology* **190**, 853–856 (1994).
62. P. D. Welch, The use of fast Fourier transform for the estimation of power spectra. *IEEE Trans. Audio Electroacoust.* **50**, 70–73 (1976).
63. M. Couade, M. Pernot, E. Messas, J. Emmerich, A. Hagège, M. Fink, M. Tanter, Ultrafast imaging of the arterial pulse wave. *IRBM.* **32**, 106–108 (2011).
64. B. Boashash, Estimating and interpreting the instantaneous frequency of a signal. I. Fundamentals. *Proc IEEE.* **80**, 520–538 (1992).
65. H. J. Vos, B. M. van Dalen, I. Heinonen, J. G. Bosch, O. Sorop, D. J. Duncker, A. F. W. van der Steen, N. de Jong, Cardiac shear wave velocity detection in the porcine heart. *Ultrasound Med Biol* **43**, 753–764 (2017).
66. R. Comolet, *Biomécanique circulatoire* (Masson, 1984).
67. S. J. Lighthill, *12. Pulse Propagation Theory in Mathematical Biofluiddynamics* (Society for Industrial and Applied Mathematics, 1975), pp. 227–252.
68. A. H. Shapiro, Steady flow in collapsible tubes. *J. Biomech. Eng.* **99**, 126–147 (1977).
69. R. L. Rockwell, M. Anliker, J. Elsner, Model studies of the pressure and flow pulses in a viscoelastic arterial conduit. *J. Franklin Inst.* **297**, 405–427 (1974).
70. C. G. Caro, T. J. Pedley, R. C. Schroter, W. A. Seed, K. H. Parker, in *The Mechanics of the Circulation* (Cambridge Univ. Press, ed. 2, 2011), pp. 1–524.

Downloaded from https://www.science.org on October 05, 2023

71. Y. Tardy, J. J. Meister, F. Perret, H. R. Brunner, M. Arditi, Non-invasive estimate of the mechanical properties of peripheral arteries from ultrasonic and photoplethysmographic measurements. *Clin. Phys. Physiol. Meas.* **12**, 39–54 (1991).
72. K. S. Rammos, G. J. Koullias, T. J. Pappou, A. J. Bakas, P. G. Panagopoulos, S. G. Tsangaris, A computer model for the prediction of left epicardial coronary blood flow in normal, stenotic and bypassed coronary arteries, by single or sequential grafting. *Vascular* **6**, 635–648 (1998).
73. M. S. Olufsen, Structured tree outflow condition for blood flow in larger systemic arteries. *J Physiol-Heart Circul Physiol* **276**, H257–H268 (1999).
74. L. Formaggia, D. Lamponi, A. Quarteroni, One-dimensional models for blood flow in arteries. *J Eng Math* **47**, 251–276 (2003).
75. S. J. Sherwin, V. Franke, J. Peiró, K. Parker, One-dimensional modelling of a vascular network in space-time variables. *J Eng Math* **47**, 217–250 (2003).
76. S. A. Urquiza, P. J. Blanco, M. J. Vénere, R. A. Feijóo, Multidimensional modelling for the carotid artery blood flow. *Comput. Methods Appl. Mech. Eng.* **195**, 4002–4017 (2006).
77. E. A. Zabolotskaya, M. F. Hamilton, Y. A. Ilinskii, G. D. Meegan, Modeling of nonlinear shear waves in soft solids. *J. Acoust. Soc. Am.* **116**, 2807–2813 (2004).
78. J.-L. Gennisson, M. Rénier, S. Catheline, C. Barrière, J. Bercoff, M. Tanter, M. Fink, Acoustoelasticity in soft solids: Assessment of the nonlinear shear modulus with the acoustic radiation force. *J. Acoust. Soc. Am.* **122**, 3211–3219 (2007).
79. S. Catheline, J.-L. Gennisson, M. Fink, Measurement of elastic nonlinearity of soft solid with transient elastography. *J. Acoust. Soc. Am.* **114**, 3087–3091 (2003).
80. G. Drzewiecki, J. J. Pilla, Noninvasive measurement of the human brachial artery pressure–Area relation in collapse and hypertension. *Ann. Biomed. Eng.* **26**, 965–974 (1998).
81. A. J. Bank, R. F. Wilson, S. H. Kubo, J. E. Holte, T. J. Dresing, H. Wang, Direct effects of smooth muscle relaxation and contraction on in vivo human brachial artery elastic properties. *Circ. Res.* **77**, 1008–1016 (1995).
82. I. Céspedes, Y. Huang, J. Ophir, S. Spratt, Methods for estimation of subsample time delays of digitized echo signals. *Ultrason. Imaging* **17**, 142–171 (1995).
83. R. Absi, Analytical solutions for the modeled k equation. *J. Appl. Mech.* **75**, 0445011–0445014 (2008).

Acknowledgments

Funding: M.T. acknowledges support from European Union's Seventh Framework Program (FP7/2007- 2013)/ERC Advanced Grant Agreement 339244-FUSIMAGINE, AXA research fund, and Fondation Bettencourt Schueller. **Author contributions:** Conceptualization: J.B., O.V., M.P., and M.T. Methodology: J.B., H.L.B., and M.T. Investigation: J.B., O.V., and G.G. Visualization: J.B. and A.D. Supervision: T.M., E.M., M.P., and M.T. Writing (original draft): J.B. and M.T. Writing (review and editing): J.B., O.V., G.G., H.L.B., T.M., M.P., and M.T. **Competing interests:** The authors declare that they have no competing interests. **Data and materials availability:** All data needed to evaluate the conclusions in the paper are present in the paper and/or the Supplementary Materials or available from the Zenodo repository at https://doi.org/10.5281/zenodo.7347982. MATLAB codes regarding the most important steps of the processing routine are also available in the same repository.

Submitted 25 April 2023
Accepted 5 September 2023
Published 4 October 2023
10.1126/sciadv.adi4252

Downloaded from https://www.science.org on October 05, 2023

Science Advances

The fundamental mechanisms of the Korotkoff sounds generation

Jerome Baranger, Olivier Villemain, Guillaume Goudot, Alexandre Dizeux, Heiva Le Blay, Tristan Mirault, Emmanuel Messas, Mathieu Pernot, and Mickael Tanter

Sci. Adv. **9** (40), eadi4252. DOI: 10.1126/sciadv.adi4252

View the article online
https://www.science.org/doi/10.1126/sciadv.adi4252
Permissions
https://www.science.org/help/reprints-and-permissions

Downloaded from https://www.science.org on October 05, 2023

Use of this article is subject to the Terms of service

Science Advances (ISSN 2375-2548) is published by the American Association for the Advancement of Science. 1200 New York Avenue NW, Washington, DC 20005. The title *Science Advances* is a registered trademark of AAAS.

Copyright © 2023 The Authors, some rights reserved; exclusive licensee American Association for the Advancement of Science. No claim to original U.S. Government Works. Distributed under a Creative Commons Attribution NonCommercial License 4.0 (CC BY-NC).